DEEP LEARNING BASED ROBUST ANALYSIS OF LASER BIOSPECKLE DATA FOR DETECTION OF FUNGAL INFECTED SOYBEAN SEEDS

MS(Research) Thesis

by

Nikhil Kaler

DEPARTMENT OF ELECTRICAL ENGINEERING

INDIAN INSTITUTE OF TECHNOLOGY INDORE

JULY 2023

DEEP LEARNING BASED ROBUST ANALYSIS OF LASER BIOSPECKLE DATA FOR DETECTION OF FUNGAL INFECTED SOYBEAN SEEDS

A THESIS

Submitted in fulfillment of the
requirements for the award of the degree
of
Master of Science (Research)

by

Nikhil Kaler

DEPARTMENT OF ELECTRICAL ENGINEERING
INDIAN INSTITUTE OF TECHNOLOGY INDORE
JULY 2023

INDIAN INSTITUTE OF TECHNOLOGY INDORE

CANDIDATE'S DECLARATION

I hereby certify that the work which is being presented in the thesis entitled "**DEEP LEARNING BASED ROBUST ANALYSIS OF LASER BIOSPECKLE DATA FOR DETECTION OF FUNGAL INFECTED SOYBEAN SEEDS**" in the partial fulfillment of the requirements for the award of the degree of **MASTER OF SCIENCE (RESEARCH)** and submitted in the **DEPARTMENT OF ELECTRICAL ENGINEERING, Indian Institute of Technology Indore,** is an authentic record of my own work carried out during the time period from August 2021 to June 2023 under the supervision of Dr. Vimal Bhatia, Professor, Indian Institute of Technology Indore, Indore, India.

The matter presented in this thesis has not been submitted by me for the award of any other degree of this or any other institute.

Nikhil
12-07-2023

Signature of the Student with Date
(Nikhil Kaler)

This is to certify that the above statement made by the candidate is correct to the best of my knowledge.

12.07.2023

Signature of Supervisor of
MS (Research) thesis with date
(Prof. Vimal Bhatia)

Nikhil Kaler has successfully given his MS (Research) Oral Examination held on

06/11/2023

M. Shaikh

Prof. Shaikh M. Mobin, Nov 6, 2023

Signature of Chairperson (OEB) with date

06.11.2023

Signature(s) of Thesis Supervisor(s) with date

13/11/2023

Signature of Convener, DPGC with date

13.11.2023

Signature of Head of Discipline with date

ACKNOWLEDGEMENTS

I would like to take this opportunity to express my heartfelt gratitude to a number of persons who in one or the other way contributed by making this time as learnable, enjoyable, and bearable. At first, I would like to thank my supervisor **Prof. Vimal Bhatia**, who was a constant source of inspiration during my work. Without his constant guidance and research directions, this research work could not be completed. His continuous support and encouragement has motivated me to remain streamlined in my research work.

I am thankful to **Prof. Abhirup Datta** and **Prof. Santosh K. Vishvakarma**, my research progress committee members for taking out some valuable time to evaluate my progress all these years. Their valuable comments and suggestions helped me to improve my work at various stages. I am also grateful to Head of Department of Electrical Engineering for his help and support.

My sincere acknowledgement to **Prof. Suhas Joshi**, Director, Indian Institute of Technology Indore for providing me the opportunity to explore my research capabilities at Indian Institute of Technology Indore.

I would like to appreciate the fine company of my dearest colleagues and friends especially, Vaibhav Mishra, Megha Nawaria, Guntupalli Keerthi, Aastha Jha, Shivani Yadav, Manish Mawatwal, Praneet Jain, Vedant Rade, Ashish Gurjar, and Anjana Sahu. Their unwavering support and camaraderie have created a pleasant and friendly environment. I am truly thankful for their companionship throughout my journey. I would like to extend my sincere thanks to my seniors at signals and Software Group (SaSg) especially, Shubham Gupta, Siddhesh Gawali, Bhagyashree Gour, Anupma Sharma, and Dr. Puneet Singh Thakur for their invaluable guidance and support throughout my MS journey. Additionally, I extend my appreciation to the wonderful individuals at the Signal Analysis Research Lab (SARL), as well as my senior Ashutosh Rajpoot, for their constant companionship and welcoming environment at IIT Indore.

I am also grateful to the Institute Staffs for their unfailing support and assistance, and the Ministry of Human Resource Development for funding the MS research.

I would like to convey my special gratitude to my father (Mr. Mahendra Singh Kaler), mother (Mrs. Manisha Kaler) and sisters (Manju and Nikita) as this thesis would not have been possible without their support encouragements and belief. Finally, I thank God Almighty to enlighten my mind for carrying out this research work

Nikhil Kaler

Dedicated To

Lord Shiva,
my family and friends

ABSTRACT

The agricultural sector holds significant global importance as it serves as a foundation for various industries, plays a crucial role in ensuring food security, and acts as a catalyst for economic growth. In India, agriculture assumes paramount significance by providing livelihood opportunities, making substantial contributions to the country's gross value added (GVA), and providing crucial economic sustenance to the low-income population. However, seed-borne pathogens, including bacteria, fungi, and viruses, significantly challenges crop production. These pathogens adversely affect seed germination and seedling establishment, resulting in low crop yields and reduced productivity. Soybean, a crucial crop worldwide, serves various purposes such as food security, animal feed, biofuel production, and sustainable agriculture. Seed-borne diseases in soybeans are transmitted through infected seeds and pose threats to plant health, vigor, and overall productivity. Enhancing productivity and satisfying global food demands depend on addressing these challenges and ensuring healthy and high-quality seeds.

Seed-borne pathogens in crops and seeds pose a challenge to high crop yields. Conventional techniques such as visual inspection, microscopic examination, seed-soaking methods, serological testing, and bioassays are used to detect these pathogens but have limitations in terms of testing time, labor, and accuracy. Modern molecular diagnostic techniques based on polymerase chain reaction (PCR) and deoxyribonucleic acid (DNA) analysis offer advantages such as rapid and specific identification of seed-borne pathogens. However, they can be expensive, labor-intensive, and destructive to samples. Non-destructive methods like near-infrared spectroscopy (NIRS), fluorescence spectroscopy (FS), Raman spectroscopy (RS), and hyperspectral imaging (HSI) provide alternatives. These techniques can detect contaminants and infections without sample destruction and have shown promise in detecting aflatoxin contamination and fungal infections. However, they also have limitations, such as interference from background elements, limited detection capabilities, and cost. Laser biospeckle technique offers advantages like high resolution, cost-effectiveness, and the ability to track biological and morphological changes in samples, making it a valuable tool for studying dynamic processes in agricultural systems.

This study uses laser biospeckle imaging combined with deep learning (DL) techniques to detect seed-borne diseases. The aim is to develop a reliable and precise model capable of analyzing biospeckle data while considering the impact of data noise on model's performance. Various DL architectures, such as neural networks, convolutional neural networks (CNNs) with long-short term memory (LSTM), three-dimensional convolutional neural networks (3-D CNNs), and convolutional LSTM (ConvLSTM), are employed to analyze the spatio-temporal aspects of the biospeckle data. The ConvLSTM model achieves an impressive accuracy of 97.72% on the test data and demonstrates robustness to different types of noise, with accuracies ranging from 94.31% to 98.86%. Additionally, the model's robustness is evaluated by varying experimental data parameters such as frame rate, frame size, and the number of frames used. The ConvLSTM model is sensitive in detecting biospeckle activity of different orders, achieving an average test accuracy of 99% for classifying four different classes. This study highlights the potential of combining biospeckle imaging and DL for the automated and accurate detection of seed-borne diseases in seeds.

Keywords: Agriculture, Biospeckle, Convolutional neural network, Deep learning, Long-short term memory, Neural network, Noise, Photonics, Seed-borne fungi.

Contents

List of Figures

List of Tables

List of Acronyms

AI Artificial intelligence.

ANN Artificial neural networks.

AUC Area under ROC curve.

AVD Absolute value of differences.

BSAI Biospeckle activity index.

CC Correlation coefficient.

CCD Charge-coupled device.

CNN Convolution neural network.

COM Co-occurrence matrix.

ConvLSTM Convolutional long short-term memory.

CRD Completely randomized design.

DL Deep learning.

DNA Deoxyribonucleic acid.

DT Decision tree.

FC-LSTM Fully connected long short-term memory.

FN False negative.

FP False positive.

FPR False positive rate.

fps frames per second.

FS Fluorescence spectroscopy.

FS Raman spectroscopy.

GD Generalized difference.

GDP Gross domestic product.

GNB Gaussian naive bayes.

GPU Graphics processing unit.

GVA Gross value added.

HSI Hyperspectral imaging.

IISR Indian Institute of Soybean Research.

IM Inertia moment.

IoT Internet of things.

kNN K-nearest neighbour.

LAMP Loop-mediated isothermal amplification.

LASCA Laser speckle contrast analysis.

LSI Laser speckle imaging.

LSTM Long short-term memory.

ML Machine learning.

MLP Multi-layer perceptron.

MSE Mean square error.

NIRS Near-infrared spectroscopy.

PCR Polymerase chain reaction.

PSNR Peak signal-to-noise ratio.

QTP Quality test protocol.

RF Random forest.

RNN Recurrent neural network.

ROC Receiver operating characteristics.

ROI Region of interest.

RTHSP Random history of speckle pattern.

SA Subtraction average.

SNR Signal-to-noise ratio.

SSI	Structural similarity index.
SVM	Support vector machine.
THSP	History of speckle pattern.
TN	True negative.
TP	True positive.
TPR	true positive rate.
UAV	Unmanned aerial vehicle.
WE	Wavelet entropy.

Chapter 1

Introduction

1.1 Importance of agriculture

Agriculture holds immense importance from a global, industrial, and economic perspective. Globally, agriculture is vital for food security, providing sustenance to a growing population. The agricultural sector also plays a crucial role in industrial production, supplying raw materials for various industries such as textiles, pharmaceuticals, and biofuels. Additionally, agriculture contributes significantly to the global economy. Achieving global development goals requires establishing healthy, sustainable, and inclusive food systems. Agricultural development is a powerful tool in eradicating extreme poverty, promoting shared prosperity, and providing nourishment for an estimated 9.7 billion people by 2050. In terms of poverty reduction, the agriculture sector demonstrates a significant advantage, with income growth among the poorest populations being two to four times higher than other sectors. Furthermore, agriculture is critical in driving economic growth, contributing approximately 4% to the global gross domestic product (GDP). In some least-developed countries, this contribution can exceed 25% of the GDP [1].

Agriculture holds immense importance from India's perspective, playing a pivotal role in its population's livelihood and economic growth. With a population of over 1.3 billion people, a significant portion depends on agriculture for their sustenance and income. According to the Annual Report 2020-21 of the Department of Agriculture, Cooperation & Farmers' Welfare, approximately 54.6% of the country's workforce is involved in agricultural and allied sector activities. Moreover, this sector contributes around 17.8% to India's gross value added (GVA) for 2019-20 [2]. Agriculture provides employment opportunities and income for millions of rural households, serving as a crucial source of livelihood.

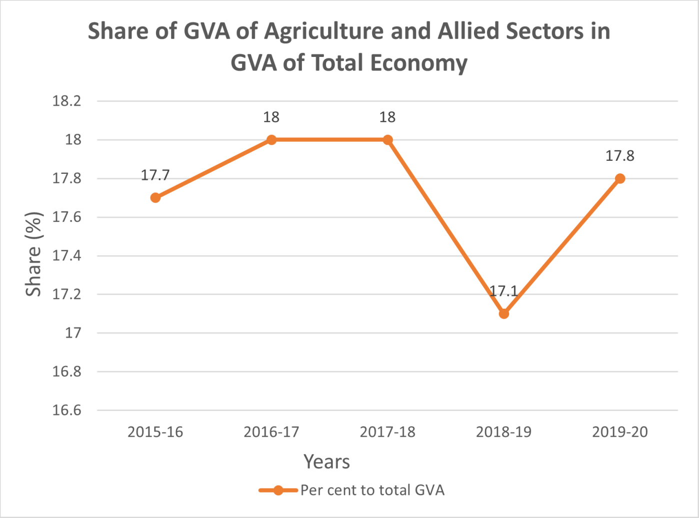

Figure 1.1: GVA of agriculture and allied sectors and its share in total GVA of the country [2].

1.2 Existing challenges in agriculture sector

Crop growth and productivity can be negatively impacted by a range of environmental challenges. These challenges can be broadly categorized into biotic stress and abiotic stress. Biotic stress refers to the harmful effects caused by living organisms such as pathogens (viruses, bacteria, fungi), pests (insects, nematodes, weeds), and other herbivores. These organisms directly affect the plant's health by depriving it of nutrients and can lead to crop losses. In response, plants have developed defense mechanisms encoded in their genetic code to counteract biotic stress. On the other hand, abiotic stress is caused by non-living factors such as extreme temperatures, drought, flooding, salinity, and mineral toxicity. These environmental factors can disrupt plant growth, development, and physiological processes. Plants have evolved various adaptive mechanisms to cope with abiotic stress, such as adjusting their water balance, modifying gene expression, and altering metabolic pathways. Biotic and abiotic stresses significantly impact plant health and can result in reduced yields, crop losses, and adverse economic consequences [3]. Understanding and managing these stresses is crucial for ensuring sustainable agricultural practices and food security in a changing climate.

Seeds play a crucial role in food crop production, as they are the source of new plants. However, the presence of seed-borne pathogens presents a significant challenge to ensuring the availability of healthy seeds. Bacteria, fungi, and viruses are examples of pathogens that can infect seeds and cause biotic stress. These pathogens negatively affect seed germination and seedling establishment, leading to weak and uneven growth and ultimately reducing crop yield [4]. Healthy seeds are vital for enhancing crop productivity and ensuring the overall health of crops.

Healthy seeds are characterized by their freedom from diseases, pests, and genetic abnormalities, enabling optimal plant growth and development. They offer numerous advantages for crop productivity improvement. Firstly, healthy seeds exhibit a higher germination rate, resulting in more successful seedlings and improved stand establishment, ultimately leading to higher yields. Secondly, using healthy seeds contributes to effective disease management by reducing the risk of introducing or spreading pathogens in the field, thus promoting healthier plants throughout the growing season. Additionally, healthy seeds possess enhanced vigor and resilience, enabling them to withstand environmental stresses like drought, heat, and cold, reducing crop losses and increasing productivity [3].

To ensure the availability of healthy seeds and promote sustainable agriculture, the development of a robust, low-cost, and industrial-level automated technique for seed identification and quality assessment is of utmost importance. Such a technique would be a standardized seed quality evaluation and health monitoring method. By implementing an automated system, identifying healthy and high-quality seeds can be streamlined, enabling efficient and reliable assessment on a large scale. Such a technique will provide farmers with accurate information about the health and viability of their seeds, saving time and resources. An automated technique would also help in detecting and managing seed-borne pathogens, ensuring that only disease-free seeds are distributed and planted. By establishing a standard for seed quality and health monitoring through an industrial-level automated approach, farmers would have access to reliable and consistent seed evaluations, leading to improved crop productivity and reduced crop losses. Moreover, such a system would enable seed producers, distributors, and regulatory bodies to maintain a high level of quality control and ensure the availability of healthy seeds to support sustainable and inclusive food systems.

1.3 Importance of Soybean in agriculture sector

Soybean holds immense significance in global and Indian economies, offering multiple benefits. With annual production exceeding 350 million metric tons in 2020, soybean is a primary protein source and accounts for 60% of total oilseed production [5]. Its contributions extend beyond nutrition, as soybean is crucial in ensuring food security by providing essential protein for human consumption and serving as high-quality animal feed. Furthermore, soybeans support the biofuel industry, contributing to sustainable agriculture and economic development. The nutritional value of soybean, coupled with increasing consumption patterns, has driven the demand for its production. Soybean has substantial oil content and high protein levels, making it a valuable source of vegetable oil and animal protein feed. Its versatility is evident in applications such as aquaculture, biofuel production, and inclusion in

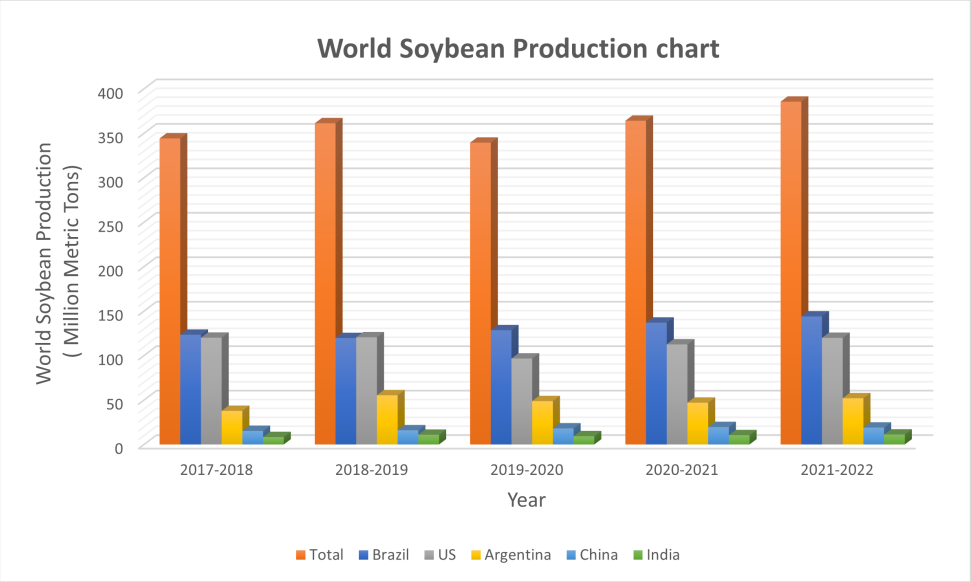

Figure 1.2: Worldwide soybean production over last five years [5].

the human diet as a protein source. Overall, soybean's importance lies in its role as a vital protein source, vegetable oil production, animal feed, biofuel production, and its potential for sustainable agriculture, making it a crop of global significance [6].

In terms of production, the USA, Brazil, Argentina, China, and India are among the leading nations, collectively accounting for over 92% of the world's soybean production [7]. Furthermore, soybean cultivation benefits from biological nitrogen fixation, reducing reliance on chemical fertilizers and promoting sustainability in agricultural systems. Ongoing research and advancements in soybean production techniques, including the use of more efficient inoculants, contribute to improving crop yields and environmental sustainability. However, seed-borne diseases pose a threat to soybean crops, as they can spread through infected seeds and lead to plant infections, reduced vigor, and decreased productivity [6]. Efforts to manage and prevent seed-borne diseases are essential for required soybean production and maintain its contributions to various sectors.

1.4 Motivation

The agricultural sector has witnessed remarkable technological advancements in recent years, significantly improving agricultural practices and crop monitoring. Integrating sensors, equipment, machines, and computers have transformed modern agriculture into a data-centric industry that requires precise and advanced data acquisition and processing technologies, ultimately enhancing productivity. New-age technologies such as artificial intelligence (AI), the Internet of Things (IoT), machine vision, robotics, and unmanned aerial vehicles (UAVs) have rapidly advanced the agricultural industry. These technologies have reshaped the agricultural sector and driven the adoption of quantitative approaches for monitoring and evaluating agricultural processes, surpassing traditional statistical methods [8].

This radical transformation in the agriculture sector has proven its importance by enhancing productivity and promoting sustainability. However, despite the significant advancements, there remains a considerable gap in implementing technological reforms in the agricultural sector, with many farming procedures and crop monitoring still reliant on conventional techniques. To bridge this gap, replacing conventional methods with photonics-based approaches and AI techniques can revolutionize the agriculture sector [9]. The monitoring of seeds and crops can be transformed by leveraging photonics sensing techniques alongside machine learning (ML) and deep learning (DL) algorithms.

This thesis explores AI's advantages in automating disease identification in seeds, specifically focusing on providing high-quality and healthy seeds to farmers at an industrial level. By leveraging AI technologies, such as ML and DL, in conjunction with laser biospeckle techniques, the agricultural industry can benefit from the automated and accurate identification of diseases in seeds. This automation streamlines the seed selection and classification process, ensuring farmers receive seeds free from diseases and other quality issues. AI techniques eliminate manual inspection and introduce efficient, data-driven approaches for disease identification, resulting in improved seed quality control and increased productivity. By embracing AI-based practices, the agriculture sector can enhance the supply chain, provide farmers with superior seeds, and ultimately contribute to the overall health and sustainability of crop cultivation.

1.4.1 Conventional methods for detection of seed-borne infection in seeds

Visual inspection, microscopic examination, seed-soaking methods, serological testing, and bioassays are conventional techniques used to determine the presence of seed-borne pathogens. Visual inspection is a simple and quick method that identifies visible signs of infection, such as discoloration or mold growth on the seeds. The microscopic examination allows for a more detailed analysis, using a microscope to observe fungal spores, bacteria, or other pathogens on or within the seeds. Seed soaking methods involve incubating seeds in a solution that encourages pathogen growth and subsequent examination for infection symptoms. Serological testing employs specific antibodies or antigens to detect pathogens based on their unique proteins or molecules, providing precise results. Bioassays utilize controlled conditions to grow seeds or seedlings and observe their response to pathogenic infection, identifying abnormalities in growth patterns or disease symptoms. However, conventional techniques for determining seed-borne pathogens are time-consuming, labor-intensive, and subjective. Visual inspection, microscopic examination, seed-soaking methods, serological testing, and bioassays have limitations such as unreliable visible signs, limited pathogen detection, inaccurate seed germination reflection, antibody availability issues, environmental influences on bioassays, and low sensitivity and specificity [10]. These limitations of conventional techniques emphasize the necessity for alternative approaches to address the challenges associated with large-scale and broad-range infection detection in seeds.

1.4.2 Molecular diagnostic techniques

Modern molecular diagnostic techniques based on polymerase chain reaction (PCR) and deoxyribonucleic acid (DNA) analysis have revolutionized the field of diagnostics, providing numerous advantages over conventional methods. These techniques include conventional PCR, nested PCR, real-time PCR, magnetic-capture hybridization PCR, and loop-mediated isothermal amplification (LAMP). They provide rapid and specific identification of seed-borne pathogens, enabling the detection of closely related organisms. Various modifications have been developed to overcome PCR inhibitors in seed DNA extracts, including using specific DNA extraction methods, adding reagents to PCR buffers, and commercial DNA extraction kits. Bio PCR, a susceptible technique, involves a pre-assay incubation step to increase the biomass of the fungal pathogen on the seeds. Nested PCR improves the sensitivity and specificity of the assay, allowing the detection of low levels of target DNA. Real-time PCR offers quantitative data and reduces the risk of cross-contamination. Magnetic-capture hybridization PCR facilitates the detection of specific DNA sequences, especially in the presence of PCR inhibitory compounds. LAMP provides a simple, cost-effective, and rapid method for specific detection of genomic DNA [11].

Despite their numerous advantages, molecular diagnostic techniques have limitations. They can be expensive, especially when selective media or commercial kits are required. Some techniques, such as nested PCR and LAMP, are more labor-intensive and prone to contamination. The detection of low levels of target fungus on seeds can lead to false negatives, and these techniques do not provide accurate information about the percentage of contaminated seeds, which is essential for seed producers and trading companies. Furthermore, the presence of compounds that inhibit DNA amplification in seeds can result in false negatives, necessitating the use of additional modifications and reagents. One additional disadvantage of molecular diagnostic techniques is their destructive nature. These methods often require the destruction of the tested sample for DNA extraction from seeds. Consequently, the sample cannot be used for other purposes, limiting its utility and potentially increasing the overall analysis cost [11].

1.4.3 Photonics in agriculture

Photonics is the branch of science and technology that deals with generating, manipulating, and detecting photons, which are entities of light. It involves studying and applying various light-related phenomena, such as emission, transmission, modulation, amplification, and detection. Photonices encompasses many technologies and devices, including lasers, optical fibers, photodetectors, sensors, and communication systems. It has numerous applications in telecommunications, information processing, medicine, manufacturing, defense, and environmental monitoring.

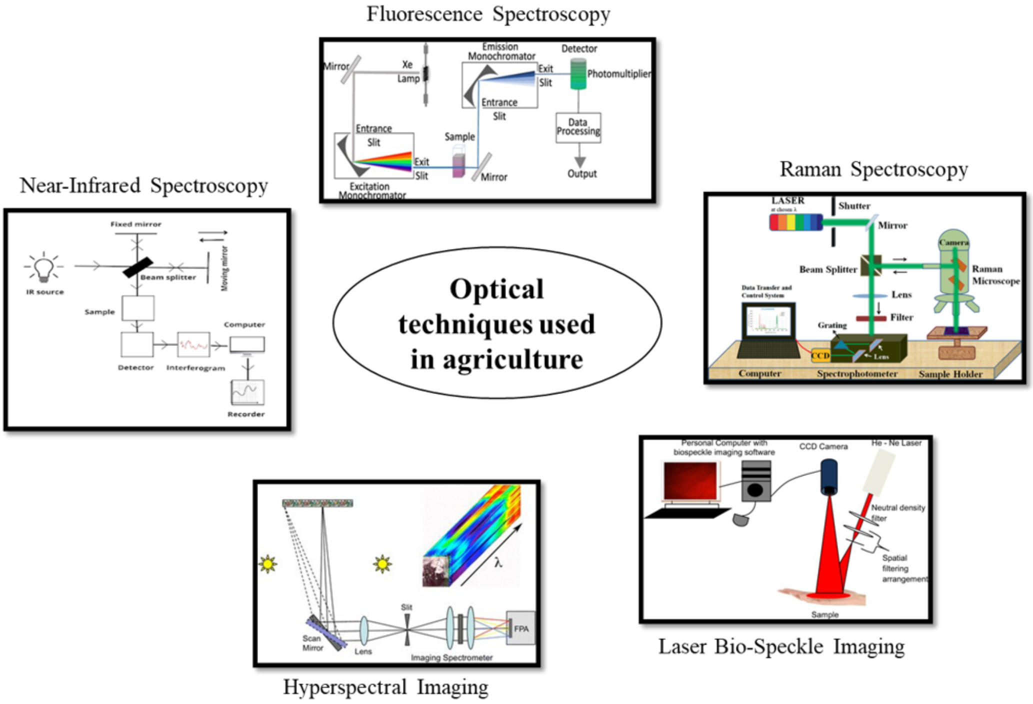

Figure 1.3: Optical techniques used in agriculture.

Non-destructive methods for the detection of contamination in a variety of agricultural products include optical techniques like near-infrared spectroscopy (NIRS), fluorescence spectroscopy (FS), Raman spectroscopy (RS), and hyperspectral imaging (HSI) [12–15]. FS has gained popularity in food science due to its ability to analyze chemical components, identify hazards, and authenticate samples. It operates by emitting light through a fluorophore upon absorbing ultraviolet or visible light. FS displays potential in aflatoxin contamination detection by leveraging the fluorescence properties of aflatoxins.

NIRS operates in the near-infrared region and detect different chemical bonds by absorption or emission of light. It has proven helpful in detecting aflatoxin contamination and fungal infection in agricultural products, and it is utilized for qualitative and quantitative evaluation of food quality and safety aspects. Chemometric techniques are often employed to interpret and analyze complex NIR spectra. HSI integrates spectroscopic and imaging techniques, simultaneously providing spectral and spatial information. It enables the mapping of chemical components in the tested sample, making it valuable for detecting unevenly distributed contaminants like aflatoxin. HSI can be implemented in different modes, such as reflectance, transmission, scattering, and fluorescence. Various methods, including point-scan, line-scan, and area-scan, acquire 3-D hypercubes of spatial-spectral data [16].

RS is a vibrational spectroscopy technique that provides spectral information through Raman's effect. It involves the scattering of light by molecules in the sample, where inelastic scattering results in energy changes and vibrational shifts. This technique allows for identifying molecular structures based on characteristic wavenumbers. RS is advantageous as it can be performed without a solvent, provides instantaneous results, and allows for intensity enhancement [14].

However, these techniques have certain limitations. In FS, the fluorescent background elements from the tested sample can interfere with the obtained aflatoxin fluorescence spectra, leading to mixed or shifted fluorescence peaks. Proper chemometric techniques are needed to handle the fluorescence spectral data accurately. NIRS relies on point detection and may have limitations in accurately detecting the inhomogeneous distribution of contaminants in different parts of the sample. Multi-point detection may be necessary for better prediction of overall contamination levels. While helpful in mapping contaminants, HSI remains expensive and has yet to be widely implemented in automatic sorting lines. Additionally, detecting low levels of aflatoxin contamination and early stages of fungal infection still presents challenges and requires further improvement through advancements in hardware, software, and chemometric techniques [16]. Furthermore, most of these techniques cannot trace the biological activity inside samples generated due to physiological and morphological changes.

The laser biospeckle technique stands out from other optical-based non-destructive techniques due to its advantages such as lower memory requirements, higher spatial and temporal resolution, cost-effectiveness, simplicity of experimental setup, and the ability to track biological and morphological changes in the sample [17]. These features make it a valuable tool for studying dynamic processes in biological systems.

1.5 Laser biospeckle technique

The laser backscattering technique is based on the speckle phenomenon, which arises when a highly coherent light source, such as a laser, illuminates an object with a diffusely reflected rough surface. This results in an interference pattern called "speckle," characterized by granular structures of dark and bright spots. Speckle

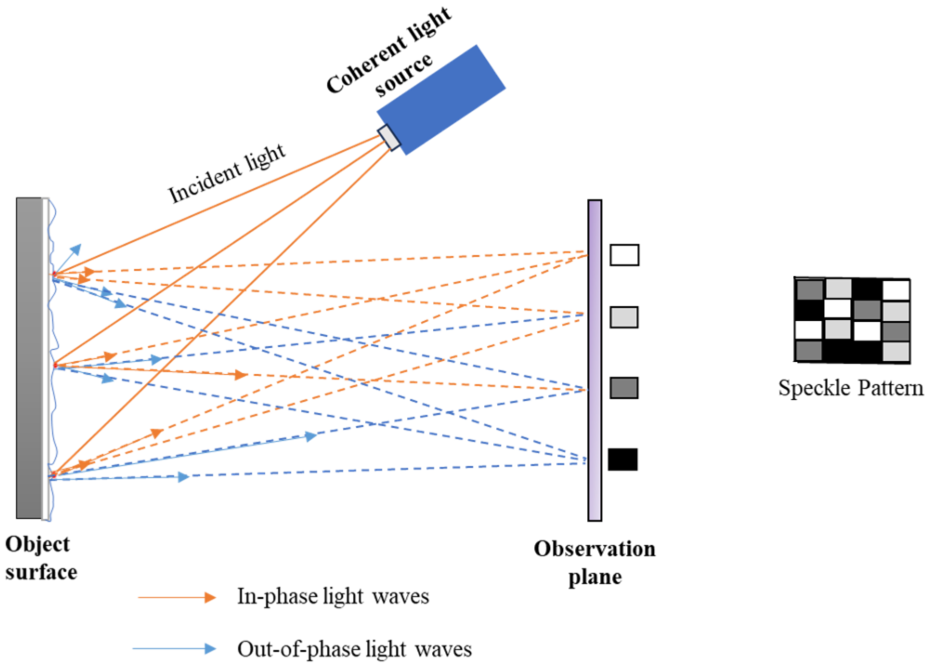

Figure 1.4: Generation of speckle pattern by a coherent light source.

formation occurs due to the interference of different light waves of the same frequency but different phases and amplitudes. The intensity changes in the speckle pattern are random and depend on the properties of the light-scattering medium. By analyzing the speckle pattern, information about deformations and changes in the illuminated surface can be obtained [18]. The speckle pattern carries a signature of biological and non-biological phenomena occurring inside the object under study, whether in a static or dynamic state. The laser backscattering technique utilizes the spatial properties of speckle images to extract valuable information about the sample under observation.

The speckle pattern observed at a specific point, $P_0(x, y, z)$, is formed by the summation of multiple components with different phase shifts $\delta\phi_n$ and amplitudes a_k scattered from various points on the field. Mathematically, the speckle signal at point P, generated by surface element k, can be expressed as [19]:

$$U_k(P_0) = \sum_{n=1}^{N} a_k e^{(i\delta\phi_n)} \tag{1.1}$$

where, $i = \sqrt{(}-1)$, and N is the total number of independent secondary wave sources generated on the illuminated surface.

The characteristics of speckles, including intensity changes, contrast, roughness, speckle grain size, and structure, as well as temporal and spatial variations of pixels, are utilized to extract valuable information from the speckle pattern. Contrast of a speckle image is calculated as [20]:

$$C = \frac{\sigma}{\langle i \rangle} \tag{1.2}$$

where $\langle i \rangle$ and σ denote the spatial average and standard deviation of the gray level intensity for each selected analysis window, respectively.

Furthermore, the size of the speckle is determined by the f-number (F) of the camera lens used in the detection system [21]. The relationship between the speckle size (S_{size}) and F is given as:

$$S_{size} = 1.22\times\ \lambda\ \times(1+M)\times F \tag{1.3}$$

where, λ is the wavelength of the laser source, and M is the optical magnification. Value of F is determined by the following equation [21]:

$$F = \frac{f}{d} \tag{1.4}$$

where, d is the size of the aperture and f the focal length of imaging lens.

The laser biospeckle phenomenon occurs when coherent laser light illuminates a biological material, resulting in a speckle pattern on an observation plane. This pattern is formed by the backscattering of light from the surface and internal inhomogeneities within the material. In the case of living organisms, the speckle pattern also includes a dynamic component caused by the movement of particles inside cells. This dynamic behavior is primarily attributed to Doppler shifts of the light interacting with these moving particles. The activity of bio speckles reflects the physical movements and absorption variations of tissue pigments, providing valuable insights into the underlying biological processes occurring within cells [20].

The experimental setup for laser biospeckle imaging includes a He-Ne laser, variable attenuator, spatial filtering arrangement, charged-coupled device (CCD) camera, and a data acquisition unit. Biospeckle patterns from the observation plane of the sample are recorded by CCD camera. The setup allows for high frame rate recording of temporal information in the speckle images. The laser backscattering technique differs as it records a single speckle image based on spatial properties. Detailed information about experimental setup and data acquisition is mentioned in Section 2.1 of Chapter 2.

In biospeckle analysis, factors like pixel saturation, under-exposure, homogeneity, camera frame rate, and contrast of the grains can affect the accuracy of calculated indexes or activity maps. A quality test protocol (QTP) is adapted to standardize these parameters and eliminate subjectivity [22]. The QTP introduces three quality parameters (saturation, contrast, and homogeneity) to ensure the acquisition of high-quality speckle images. This protocol helps obtain the best quality images for accurate analysis and interpretation in biospeckle studies.

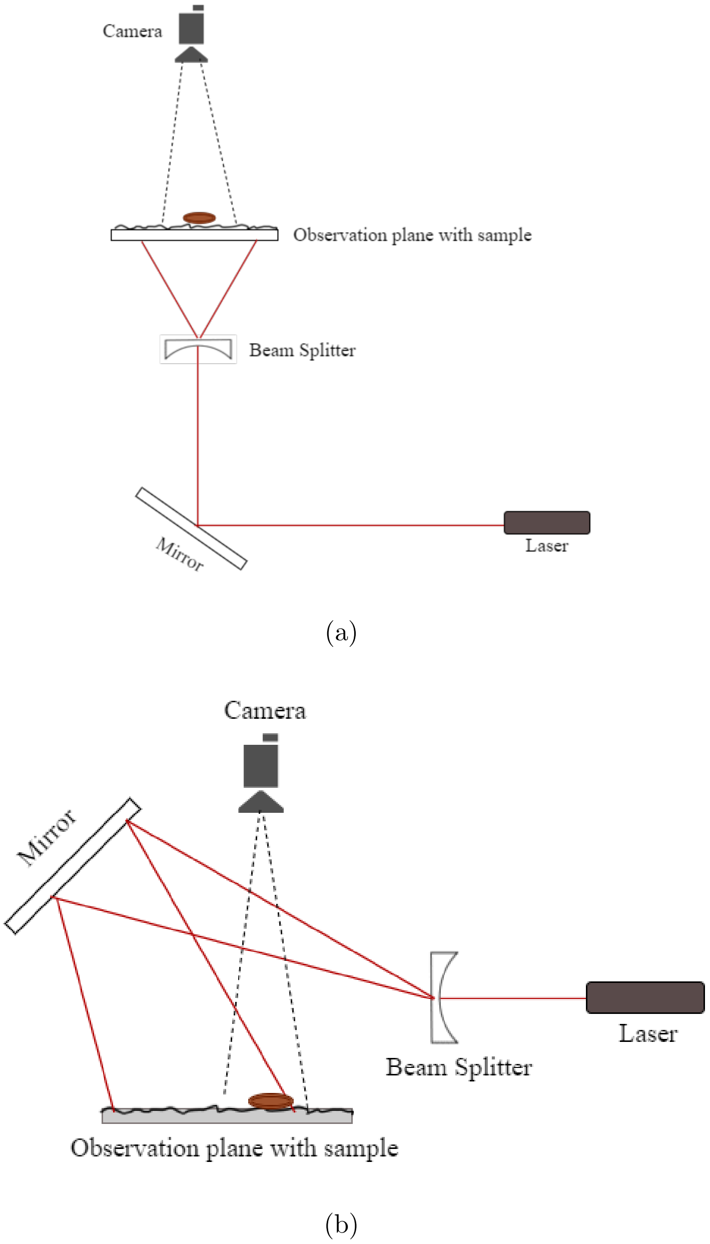

(a)

(b)

Figure 1.5: Experimental setup for laser biospeckle imaging (a) Forward scattering arrangement (b) Back scattering arrangement.

1. **Saturation:** This test determines if any portion of the image is underexposed or saturated. Saturation occurs when pixels have values of either 0 or 255, representing the lower and upper levels of the grayscale, respectively. Identifying saturated areas is crucial because they can compromise the accuracy of the analysis. This parameter is calculated by dividing speckle images into small windows of pixel size M×N and classifying the image areas into saturation, normal, and sub-exposition based on pixel values. Discarding saturated or sub-exposed speckles and readjusting parameters is essential for optimal results.

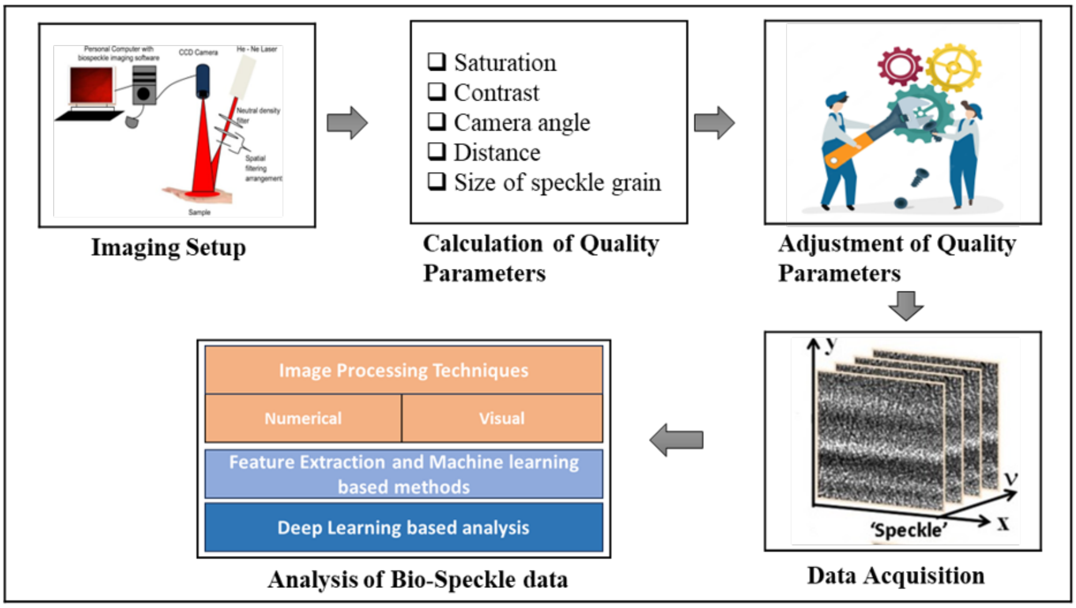

Figure 1.6: Steps involved in biospeckle data analysis.

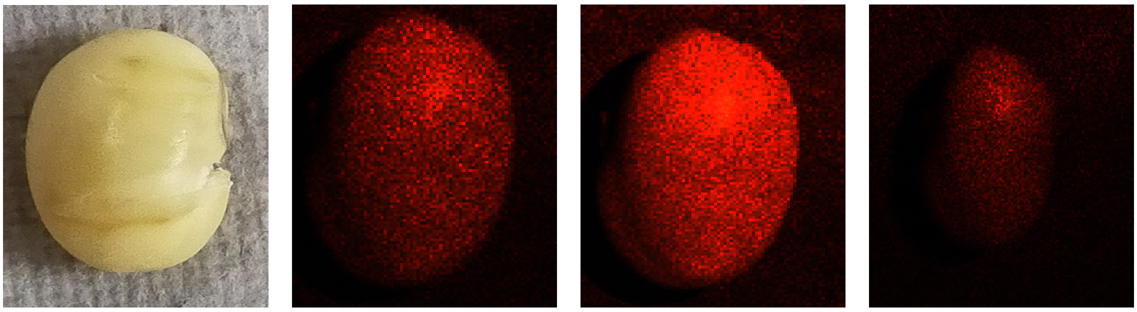
(a) (b) (c) (d)

Figure 1.7: (a) Image of soybean seed, (b) high quality, (c) over-exposed, and (d) under exposed speckle image.

2. **Contrast:** Contrast is a measure of activity in the speckle pattern. It evaluates the integration period of the camera and provides information about the activity of the material under observation. The test assesses the contrast of the speckle grains in a single image to ensure that the activity is adequately expressed. Low contrast indicates a higher velocity of the monitored phenomenon than expected, leading to potentially erroneous conclusions during the image analysis. Contrast of speckle image is calculated by using the Equation 1.2.

3. **Homogeneity:** This test assesses the level of homogeneity in the whole image. It identifies areas where the activity measured by numerical methods (such as inertia moment (IM) [23] or absolute value of difference (AVD) [24]) differs significantly from the borders of areas with different activities. The test helps associate graphical and numerical results by evaluating homogeneity, particularly when analyzing heterogeneous samples.

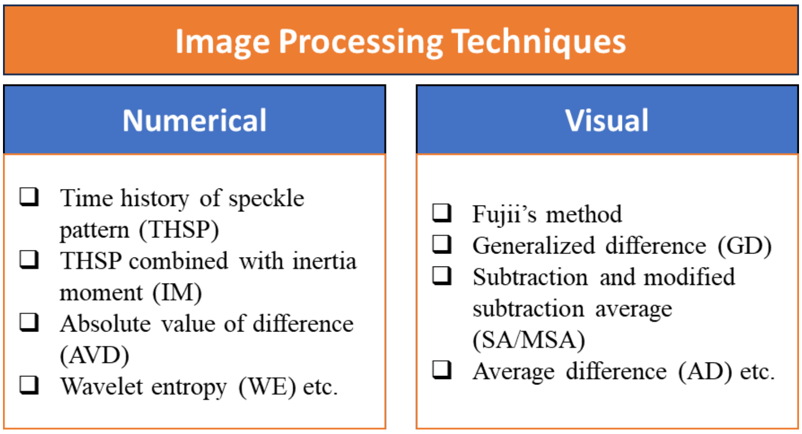

Figure 1.8: Image processing-based methods.

1.5.1 Image processing-based methods for assessment of biospeckle data

The two methods commonly used in literature to examine the dynamicity of a biospeckle pattern are numerical indexing and visual inspection-based methods.

1. **Numerical techniques:** Numerical indexing techniques are commonly used to analyze and quantify activity levels in biospeckle patterns. Popular techniques are random time history of speckle pattern (RTHSP) [25] and RTHSP combined with IM [26], Wavelet Entropy (WE) [27], Correlation Coefficient (CC), and AVD. THSP is created by arranging successive images of dynamic biospeckle phenomena, with each image contributing a column of pixels placed side by side. The resulting matrix represents the time evolution of biospeckle intensity fluctuations. IM is calculated using a co-occurrence matrix (COM) derived from the THSP. The COM shows the spread of non-zero values, with low activity concentrated around the diagonal and high activity resembling a cloud. The IM is defined as the sum of the matrix values multiplied by the squared distance from the principal diagonal.

   An alternative method to IM is AVD, which calculates the absolute value of the distance from the principal diagonal. AVD aims to avoid the potential distortion caused by the square operation in the IM method. It has shown better results in some cases of biospeckle activity, particularly when the THSP matrix has no data at high frequencies. WE is another indexing technique proposed for dynamic speckle phenomenon analysis. It measures the order and disorder in a multifrequency signal of speckle activity. Each row of the THSP is treated as an individual time series, and the mean value of WE from all rows is calculated as a single image descriptor. WE method has demonstrated better agreement with experimental data compared to IM for changes in low-frequency biospeckle patterns.

From experimentally recorded biospeckle data, RTHSP and COM for healthy and diseased sample are represented in Figure 1.9.

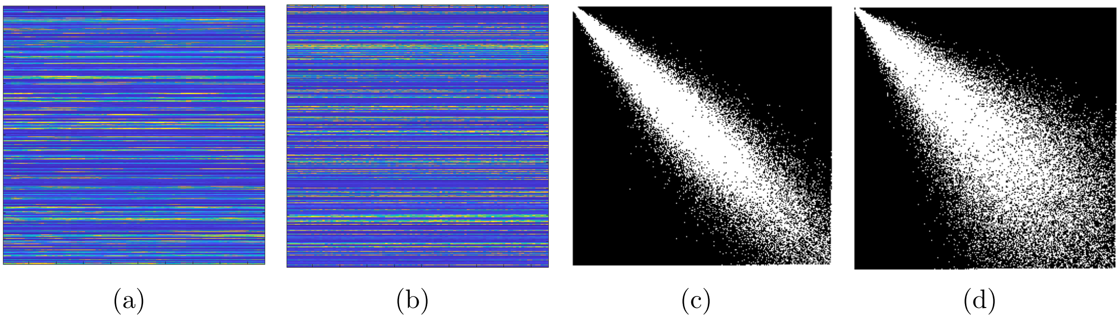

Figure 1.9: RTHSP for (a) healthy seed sample, (b) diseased seed sample ; COM for (c) healthy seed sample, (d) diseased seed sample

2. **Visual methods:** Visual analysis of biospeckle activity involves using various full-field indexing techniques that utilize every pixel of each speckle frame to assess the activity. These visual analysis methods offer higher accuracy, zero standard deviation, and the ability to handle homogeneous and heterogeneous activities. Here are some of the commonly used visual analysis techniques:

   (a) **Fujii's Method:** Fujii's method calculates a weighted sum of the differences between two consecutive elements of the time sequence of intensities for each pixel. The resulting index represents regions of high and low speckle intensity while preserving the contours of the tested object. However, this method may produce false activity in darker regions due to the nonlinear response and can be improved by using frequency decomposition with wavelet transform [28].

   (b) **Generalized difference (GD):** The GD method eliminates the weighting process and calculates the cumulative sum of absolute differences between pixel intensities among all frames. It includes differences between non-consecutive frames, but the appearance order is not considered. The resulting activity map shows the spread of values without temporal information about the frequency of transitions [29].

   (c) **Laser speckle contrast analysis (LASCA):** LASCA is based on calculating spatial or temporal contrast over a local window of pixels. The contrast value is computed for each pixel using a moving window, and the resulting values are averaged or smoothed. LASCA can be derived from a single image or a set of collected frames. The method is computationally fast and is suitable for real-time monitoring but results in a loss of resolution [30].

(d) **Subtraction average (SA):** SA algorithm is used to process the image sequence. It calculates the absolute difference between the pixels of two consecutive images I_k and I_{k-1} and sums them up. This generates a 2-D visual activity map ($\mathrm{SA}(x,y)$) that represents the spatio-temporal variations in the sample. A numerical index (A'_{SA}) is presented to quantify the overall dynamic activity by taking the spatial average of the complete activity map. Based on the SA algorithm, this index provides a measure of the overall dynamism of the sample [31]. This method is used in Section 2.3 to find order of biospeckle activity in different samples. Mathematical equations for $\mathrm{SA}(x,y)$ and A'_{SA} are given as:

$$\mathrm{SA}(x,y) = \sum_{k=1}^{n} |I_k(x,y) - I_{k-1}(x,y)| \tag{1.5}$$

$$A'_{\mathrm{SA}} = \frac{1}{(r \times c)} \sum_{x=1}^{r} \sum_{y=1}^{c} \sum_{k=1}^{n} |I_k(x,y) - I_{k-1}(x,y)| \tag{1.6}$$

where k is image sequence index, x and y are the coordinate of image I_k, r is the number of rows, and c is the number of columns of 2-D visual activity map ($\mathrm{SA}(x,y)$).

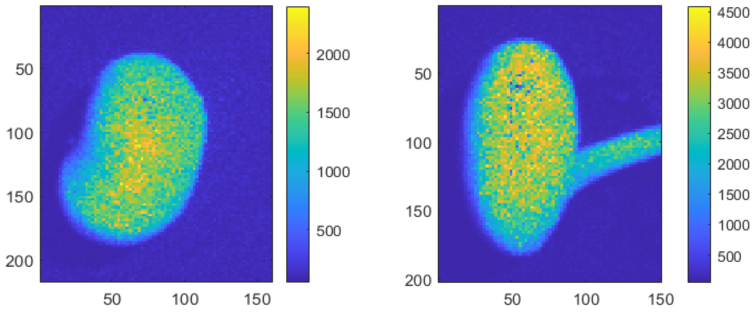

(a) (b)

Figure 1.10: Visual activity map for soybean seeds (a) healthy sample , (b) diseased sample.

Numerical methods used in the biospeckle analysis have limitations such as the inability to handle sample inhomogeneity, low sensitivity towards low and medium activity levels, high standard deviation, and manual procedures for analysis. They also depend on the type of sample being analyzed, which can limit their applicability. On the other hand, visual methods suffer from disadvantages such as manual region of interest (ROI) selection, dependence on various experimental conditions, reliance on temporal variations of speckle frames, and sensitivity to the shape and size of the sample. Manual ROI selection is prone to human error, while automatic selection requires higher computational time and power. Undesired background noise can lead

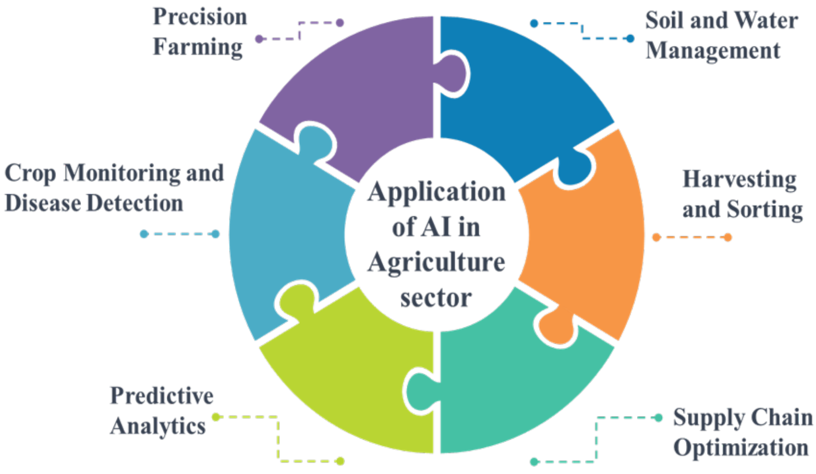

Figure 1.11: Artificial intelligence and its application in agriculture.

to false ROIs and erroneous activity measurements. Most visual techniques provide only qualitative information and lack quantitative measures of activity, making them unsuitable for comparing samples over different time durations. Extracting numerical values from visual techniques adds complexity and computation time to the analysis procedure. Both numerical and visual methods have limitations that restrict their accuracy and applicability in biospeckle analysis.

1.6 Artificial intelligence in agriculture

AI refers to developing intelligent machines that can simulate human-like intelligence and perform tasks that typically require human intelligence, such as learning, reasoning, problem-solving, and decision-making. AI finds various applications in agriculture and offers solutions to improve productivity, efficiency, and decision-making. Through precision agriculture, AI helps farmers optimize crop selection, irrigation, pest control, and harvesting by utilizing sensor data and monitoring systems. It enables real-time monitoring of weather conditions, soil health, and crop growth. AI-powered drones and robots assist in crop monitoring, data collection, and labor-intensive tasks. Predictive analytics and forecasting enable businesses to anticipate pricing trends, manage supply chains, and optimize production. With its ability to process and interpret large amounts of data, AI empowers farmers to overcome traditional challenges, increase productivity, and meet the demands of a growing global population [32].

AI revolutionizes image and data processing by leveraging its ability to learn from large datasets and identify complex patterns. AI algorithms such as ML and DL in image processing enable automatic feature extraction, object classification, and anomaly detection with enhanced precision and speed. In data processing, AI handles diverse datasets, extracting valuable insights and making accurate predictions. It excels in processing unstructured and complex data, such as sensor data

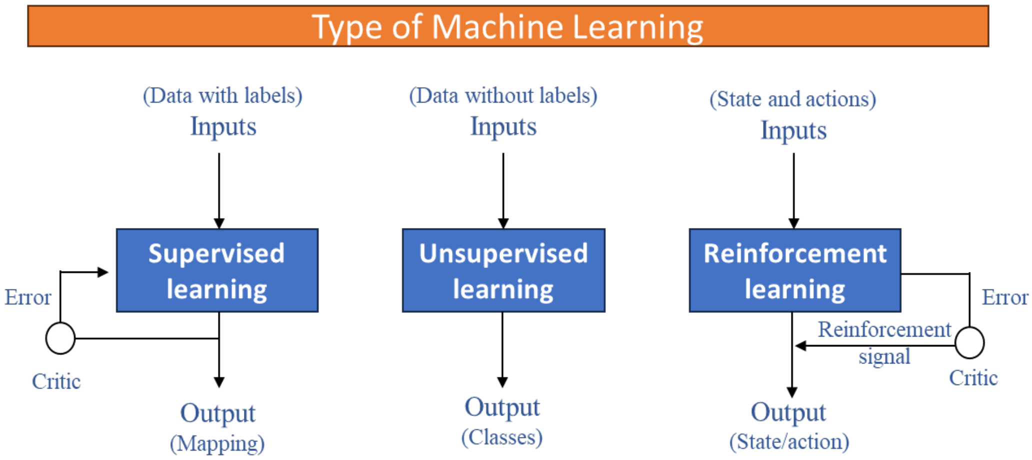

Figure 1.12: Type of machine learning.

or satellite imagery, enabling real-time and comprehensive analysis. AI automation reduces manual effort and errors while continuously improving performance.

The laser backscattering technique analyzes speckle images based on their spatial properties, such as intensity changes, contrast, roughness, and size of speckle grains. Manually extracting limited features from speckle images is inadequate for accurately characterizing biological samples. Visual and numerical analysis methods analyze the dynamicity of the samples, but they have limitations and are influenced by various experimental and processing factors. To address these challenges and minimize subjective biases, a processing pipeline leveraging ML and DL techniques has been developed. These algorithms enhance accuracy and eliminate subjectivity by automatically extracting and analyzing intricate patterns in speckle images.

1.6.1 Machine learning

ML is a fundamental component of AI that focuses on developing algorithms and models capable of learning from data and making intelligent decisions without explicit programming. It is a subset of AI that enables systems to automatically analyze and interpret data, identify patterns, and make predictions or actions based on the learned patterns. ML algorithms use statistical techniques to iteratively learn from data, improve performance, and adapt to new information or changing environments.

Three primary types of machine learning algorithms are supervised, unsupervised, and reinforcement learning. Supervised learning involves training a model with labeled examples to make predictions or classifications. The algorithm learns from the input-output pairs provided during training and then predicts the output for new, unseen inputs. On the other hand, unsupervised learning deals with unlabeled data and aims to discover patterns or structures within the data without explicit guidance. It involves clustering data points based on similarities or finding hidden patterns. Reinforcement learning involves an agent learning to interact with an environment through trial and error. The agent receives feedback through rewards or penalties, allowing it to learn optimal actions to maximize its cumulative reward over time [33]. These three types of machine learning algorithms provide a foundation for various applications and enable systems to learn from data, make informed decisions, and adapt to different scenarios.

ML-based analysis of biospeckle data has been used in the agriculture sector for various applications, including early identification of seed fungal infection [34], detection of chilling and freezing disorders in orange [35] and seed viability assessment [36]. ML automates decision-making process by extracting features from data. However, the traditional approach of manually crafting features is time-consuming, semi-automated, and limited to known features. It requires expert knowledge and is susceptible to noise, leading to decreased performance of ML models in noisy environments. DL-based end-to-end models offer process automation and enhanced model robustness.

1.6.2 Deep learning

DL-based methods have the advantage of automated feature extraction and decision-making processes by allowing the model to learn and extract valuable features directly from the data. This eliminates the need for manual feature extraction techniques, which can be subjective and limited in their ability to capture complex patterns. DL-based analysis of biospeckle data has been used to assess seed quality [17] and detection of defects in apples [37]. These studies have utilized DL-based methods that leverage spatial information from a single speckle frame. However, using only a single speckle frame for the biospeckle activity assessment is prone to noise and lacks the dynamic component of biospeckle activity for its assessment.

This investigation aims to develop a non-destructive, real-time automated technique for detecting fungal-infected soybean seeds using a combination of DL and laser biospeckle technique. The objectives of this study include developing DL-based spatio-temporal analysis on biospeckle data using different models, evaluating the models' robustness against noise in data acquisition, assessing the impact of experimental parameters (such as frame size, frame rate, and number of frames) on the performance of the best robust model, and extending the model to detect the biospeckle activity of different orders in multi-class data. This research highlights the potential of DL-based methods in real-time seed contamination detection, offering promising applications in agriculture.

1.7 Thesis outline and contributions

This thesis is organized in 4 chapters, which are briefly described with their contributions as follows:

Chapter 1. Introduction: This chapter highlights the significance of agriculture, the challenges posed by stress factors in crop production, and the need for effective seed infection detection methods. It discusses the limitations of conventional and molecular diagnostic techniques currently used in agriculture. It also introduces the motivation behind the thesis and proposes utilizing photonics techniques and artificial intelligence as potential solutions.

Chapter 2. Data acquisition and deep learning based spatio-temporal analysis of biospeckle data: This chapter focuses on the experimental setup, data acquisition process, and the addition of noise in the test data. It introduces a DL-based strategy for the spatio-temporal analysis of biospeckle data and describes various DL-based networks and models developed for the analysis.

Chapter 3. Result and discussion: This chapter presents the results of ML and DL models, including the classification of healthy and diseased seeds using ML, the performance and robustness of various DL models, the evaluation of the best robust model under different experimental parameters, and the sensitivity analysis of the best model for the biospeckle activity of different orders.

Chapter 4. Conclusions and Future Works: This chapter summarizes the thesis contributions, highlighting key insights and significant observations. Conclusions are drawn based on the findings, and the future scope of work is discussed, indicating potential areas for further research and development.

Chapter 2

Data acquisition and deep learning based spatio-temporal analysis of biospeckle data

2.1 Experiment setup and data acquisition

Majority of anthracnose disease in soybean seeds is caused by the seed-borne fungus *Colletotrichum truncatum* (*C. truncatum*) [38]. In this study, we obtained 1000 soybean seeds of JS 20-29 variety from the ICAR-Indian Institute of Soybean Research (IISR) plant field in Indore, India. These seeds underwent a series of treatments for experimental purposes. First, they were disinfected using a solution of sodium hypochlorite and distilled water in equal proportions. Then, they were surface sterilized with distilled water and dried at room temperature on sterilized filter paper. Further, these seeds were divided into two groups; one was healthy, and the other was infected with *C. truncatum.* The experiment followed a completely randomized design (CRD) and consisted of five replications, each containing twenty seeds. A 20 ml spore solution of *C. truncatum* with a concentration of 10^6 was uniformly applied to the seeds to induce infection in the diseased seed group.

The experimental setup arrangement is shown in Figure 2.1, which consists of a He- Ne laser source (wavelength = 632.8 nm and power = 15 mW), variable attenuator, spatial filtering arrangement (microscopic objects (m= 40X and aperture= 10 μm), collimation lens), and CCD camera (Basler Corp., frame rate= 32 frames per sec (fps); resolution= 1294x964). A spatial filtering arrangement creates a filtered and enlarged laser beam by applying beam-filtering techniques to suppress noise components. A neutral density filter (Thorlabs, USA) is employed to absorb light in the visible and near-IR range, reducing the optical power of the incident beam. This ensures the samples are neither under nor over-exposed, preventing inaccurate results. A precision achromatic doublet lens with specific parameters (focal length = 250 mm, diameter = 50 mm) collects and focuses the expanded laser beam. Vibration-isolation tabletop is utilized during the experimental setup to mitigate errors caused by vibrations from the surrounding environment.

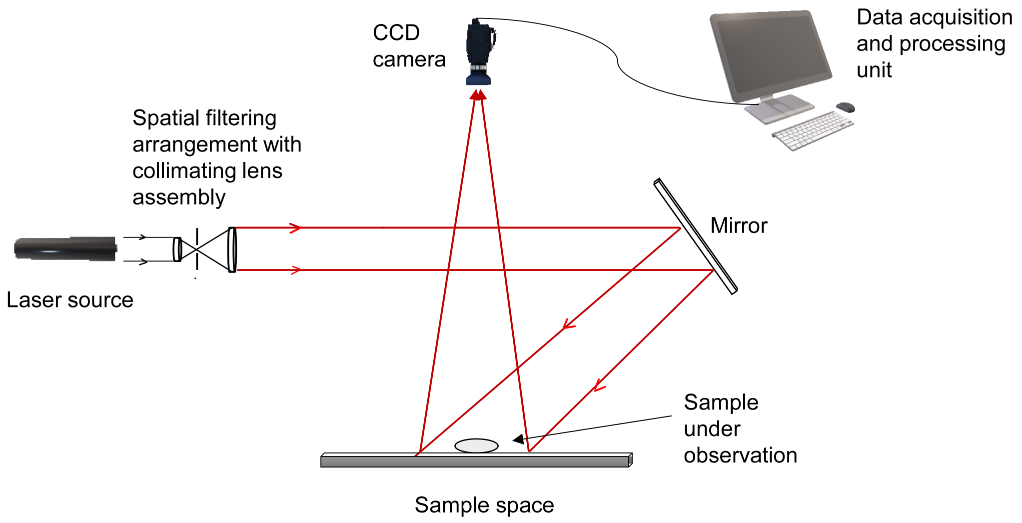

Figure 2.1: Experimental setup for data acquisition.

The laser was used to illuminate seed samples, and a camera lens captured the resulting backscattered light. A high frame rate CCD camera was employed to capture sequential speckle images at different time intervals for each sample. Quality characteristics, such as contrast and saturation, are significantly influenced by the recording angle and size of the speckle grain, which directly affects the biospeckle activity [39]. Therefore, these quality parameters were optimized before data acquisition. Block diagram in Figure 2.2 represents the data acquisition process. Biospeckle activity within healthy and diseased samples exhibits different orders due to variations in physiological and biochemical processes inside the samples. Some initial frames from the biospeckle image stack for both sample types and the original sample images are shown in Figures 2.3 and 2.4, respectively.

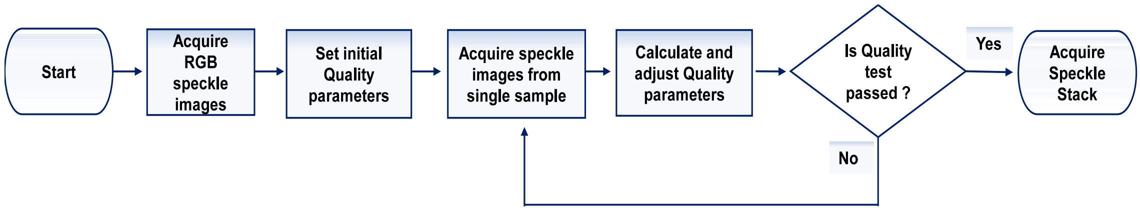

Figure 2.2: Block diagram for data acquisition process.

(a) (b)

Figure 2.3: Original images of samples.

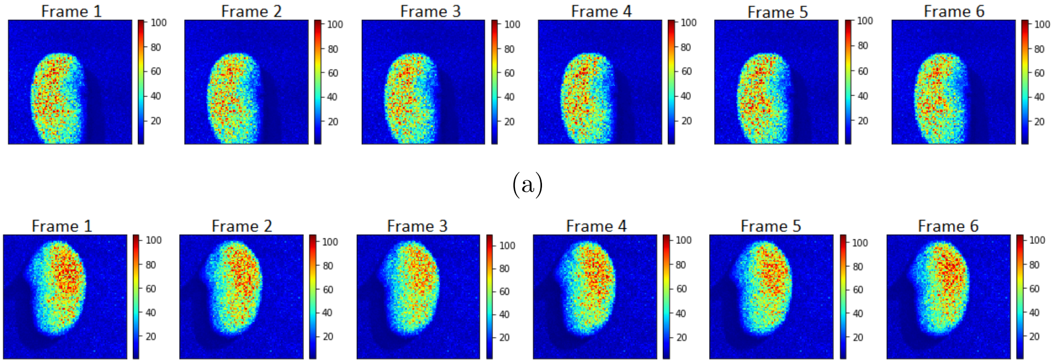

(a)

(b)

Figure 2.4: Temporal variation in recorded speckle frames for (a) healthy sample (b) diseased sample.

2.2 Noise addition and noised test data preparation

The quality of a laser image can be affected by several factors, including the sensitivity of intensified CCDs, atmospheric turbulence, laser energy, structural characteristics of the optical receiving system, and non-uniformity of the illumination. These factors can reduce the signal-to-noise ratio (SNR), resulting in decreased contrast and brightness, which poses challenges to the quality of speckle images and results in noise addition. There are mainly three types of noises (impulsive noise, Gaussian noise, and speckle noise) that affect the image quality in laser active imaging systems [40].

In Laser Speckle Imaging (LSI), the formation of speckle patterns is primarily influenced by multiple backscattered and forward scattering of light, which introduce random delays in the propagation of the forward and returning beams. Temporal coherence of the light source, phase aberrations, and detector's aperture are other factors affecting speckle patterns. The resulting speckle image in LSI contains both noise and information. Noisy speckle patterns reduce intensity variations and hinder the correspondence between local density scatters, limiting the visibility of small, low-contrast structures within the speckle pattern [41].

CCD photosensors undergo multiple stages of signal conversion to transform incident photons into digital signals. This conversion process involves converting photons-to-electrons, electrons-to-voltages, and voltages-to-digital signals. However, at each conversion stage, several noises get introduced, including photon shot noise, dark current noise, sense node reset noise, and non-linear behavior of gain values. Photon shot noise arises from the random nature of photon detection, while dark current noises result from thermal effects in the sensor. Sense node reset noises occur during charge resetting, and non-linearity refers to deviations from an ideal linear response. These noise sources can introduce fluctuations, background signals, variations in charge level, and distortions in the sensor's response, impacting the accuracy and fidelity of captured images or signals. When creating simulation models for CCD photosensors, these noise sources are typically represented using probability distributions such as Poisson, Gaussian, log-normal, and inverse Gaussian distributions [42]. These distributions help to accurately model the random nature and characteristics of the noise introduced during the signal conversion stages in CCD photosensors.

The noise in data can significantly impact the performance of DL based models. To assess the robustness of the model, four additional test datasets were created by adding spatial noises to the biospeckle video frames of the original test data. These noise-added test datasets are described as follows:

2.2.1 Gaussian noised test dataset

Gaussian noise is added to each pixel in the image by summing random values from a Gaussian distribution with the actual pixel values [43]. The probability density function (PDF) of Gaussian noise is mathematically represented by a normal distribution which is given as:

$$P(g) = \frac{1}{\sigma\sqrt{2\pi}} e^{\frac{-(g-\mu)^2}{2\sigma^2}}, \tag{2.1}$$

where g is the noise pixel gray value, μ and σ are the mean and standard deviation, respectively.

2.2.2 Salt and pepper noised test dataset

Salt and pepper noise, also known as impulsive noise, is added to the image by randomly inserting bright (255-pixel value) and dark (0-pixel value) values throughout the image. Salt and pepper noise is represented as [43] :

$$P(g) = \begin{cases} P_a & \text{if } g = a \\ P_b & \text{if } g = b \\ 0 & \text{if } otherwise \end{cases}, \tag{2.2}$$

where $P(g)$ is the PDF, P_a and P_b represent two peak values in PDF at low gray level 'a' (high pixel value region) and high gray level 'b' (low pixel value region), and g is the pixel gray value.

2.2.3 Speckle noised test dataset

Speckle noise is a multiplicative noise generated by multiplying random pixel values with different pixels of the image. It is represented by a combination of the original image and Gaussian-distributed noise as:

$$K\left(i,j\right) = I\left(i,j\right) + N\left(i,j\right) \times I\left(i,j\right), \tag{2.3}$$

where $I\left(i,j\right)$ is the original image, $K\left(i,j\right)$ is speckle noised image, and $N\left(i,j\right)$ is Gaussian distributed noise.

2.2.4 Multiple noises added test dataset

This test dataset is prepared using multiple noises considered for modeling of CCD photosensor. Image $I\left(i,j\right)$ is used as the λ parameter for generating Poisson random numbers to simulate shot noise in the sample frames. Furthermore, Poisson noised test samples are added with log-normal and Gaussian-distributed noises.

The PDF of log-normal distributed noise is given as:

$$P_X\left(x\right) = \frac{1}{x\sigma'\sqrt{2\pi}}\exp\left(-\frac{\left(\ln(x)-\mu'\right)^2}{2\sigma'^2}\right), \tag{2.4}$$

where μ' and σ' are mean and standard deviation of the natural logarithm of random variable X, respectively.

The PDF of Poisson distributed noise is given as:

$$P\left(X=k,\lambda\right) = \frac{e^{-\lambda}\,\lambda^k}{k!}, \tag{2.5}$$

where λ is the mean number of events, and k is the number of occurrences.

Parameters such as SNR, peak signal-to-noise ratio (PSNR), mean square error (MSE), correlation coefficient (CC), and structural similarity index (SSI) can be used to analyze the effects of noise in the images [41]. These parameters are calculated, and their mean values across all sample frames are used to evaluate the extent and impact of noise addition in the test samples. Table 2.1 provides the values of these parameters for a single sample from different noise-added test datasets. Figure 2.5 depicts the changes in pixel intensity values for a single frame in the sample. Figure 2.6 represents the number of pixels affected by adding different noises through histogram plot. These noise-added test datasets allow for robustness analysis and evaluation of DL models under varying noise conditions, providing insights into the model's performance and ability to handle noisy input data.

Noise Used	Signal-to-Noise Ratio (SNR(dB))	Peak Signal-to-Noise Ratio (PSNR(dB))	Correlation Coefficient (CC)	Mean Square Error (MSE)	Structural Similarity Index (SSI)
Gaussian noise	14.440	30.656	0.957	55.899	0.7196
Salt and pepper noise	4.715	20.930	0.736	526.30	0.6402
Speckle noise	10.025	26.240	0.8985	154.537	0.7325
Multiple added noise	15.053	31.273	0.968	48.47	0.7931

Table 2.1: Numerical quantification of noise addition using different parameters for noised test dataset samples.

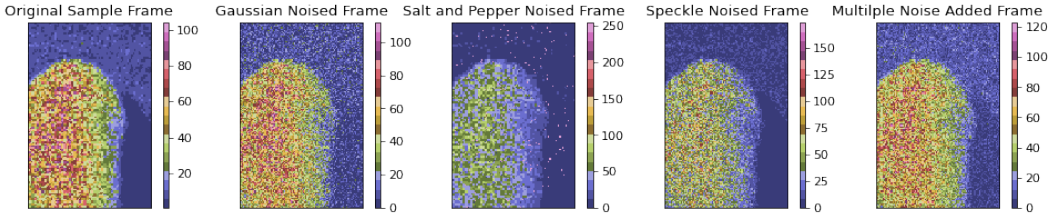

Figure 2.5: Effect of adding different noises on pixel values in a single frame of a test sample.

2.3 Synthetic biospeckle data generation to extend the dataset to multi-class

A model is said to be sensitive to the detection of biospeckle activity if that can easily identify the biospeckle activity of different orders. To evaluate the sensitivity of the model, the dataset is extended to multi classes by generating synthetic data. The biospeckle activity is quantitatively measured using the biospeckle activity index (BSAI), calculated using the subtraction average algorithm [44]. The BSAI values of healthy and diseased samples are determined. To create additional classes with higher BSAI values, the standard rotating diffuser model [45] is utilized. This model

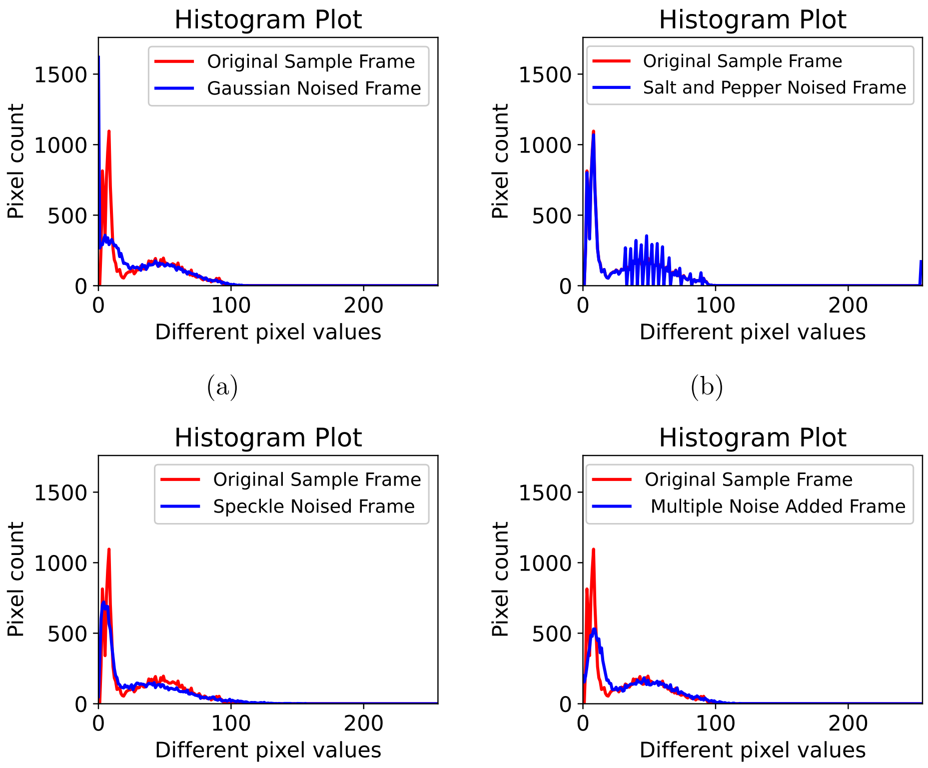

(a) (b)

(c) (d)

Figure 2.6: Histogram plot for different noise addition in a single frame of a test sample.

allows the generation of virtual biospeckle specimens that resembles original samples. The steps for the generation of synthetic speckle patterns are as follows:

1. Generate a speckle pattern using the equation:

$$I_1\left(a,b\right) = FT^{-1}\left\{H \times FT\left\{e^{j\times\varphi(a,b)}\right\}\right\}, \tag{2.6}$$

   where a, b are the pixel coordinates, H is the coherent transfer function, $FT^{-1}\{.\}$ and $FT\{.\}$ denote inverse and direct Fourier transform respectively, and $\varphi\left(a,b\right) \in [0, 2\pi]$ is random phase matrix.

2. Rotate each generated speckle pattern by an angle to introduce variation in the correlation between speckle images in a stack S.

$$S = [I_1, I_2, I_3, \ldots,\ I_n] \tag{2.7}$$

   For H = 250, we get a synthetic speckle pattern of frame size=200x200 with 96 frames. Table 2.2 represents the experimental data and two extended classes with their BSAI values.

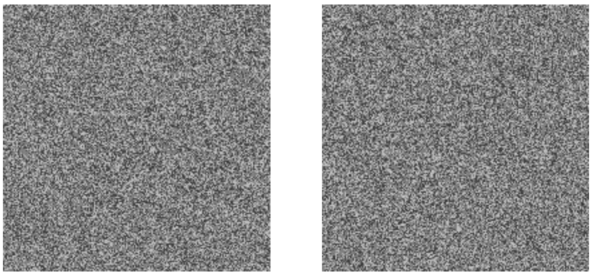
(a) (b)

Figure 2.7: Artificial speckle pattern generated through mathematical modeling for (a) Class 2 and (b) Class 3

	Experimental data		Synthetic data	
	Healthy samples (Class 0)	Diseased samples (Class 1)	Class 2	Class 3
Approx. BSAI ($\times 10^3$)	0.5-0.8	1.0-1.6	2.0-2.6	3.3-3.8
Samples	300	300	240	240

Table 2.2: Four class dataset having biospeckle activity of different orders.

2.4 Spatio-temporal analysis of biospeckle data using supervised learning algorithms

For our work, we used supervised learning to develop ML and DL models. Figure 2.8 shows the typical workflow for implementing the supervised learning process to classify the labeled data. The process of supervised learning involves several essential steps. First, the dataset is prepared by dividing it into training, validation, and testing sets, ensuring the labels are correctly assigned to the corresponding input features. Then, a suitable model is selected based on the problem, such as linear regression, decision trees, or neural networks. The model is initialized with random parameters and trained on the labeled training data through an iterative process known as optimization, where it adjusts its parameters to minimize the difference between predicted and actual labels. This is done by applying a chosen optimization algorithm and a loss function that quantifies the model's performance. Once the model is trained, its effectiveness is evaluated using the testing set to assess its performance on unseen data. If the performance is satisfactory on the evaluation matrices, the model can be deployed to make predictions or classifications on new, unlabeled data [33]. Regularization techniques and hyperparameter tuning are often applied to improve the model's accuracy and prevent overfitting, which can be monitored using the model's performance on validation data.

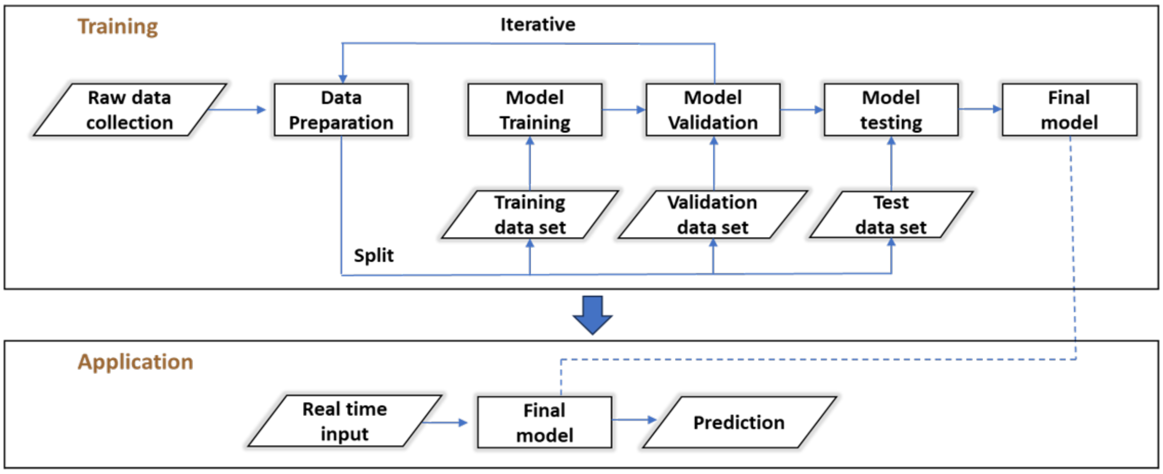

Figure 2.8: Overall workflow of supervised learning process.

2.4.1 Machine learning based classification

ML-based processing involves several steps, including data pre-processing, feature extraction, predictive model development, and evaluation. Speckle frames are pre-processed by removing unwanted spatial information to convert frame size to 150 × 100. Spatial and temporal features such as temporal AVD, contrast, entropy, roughness, IM, and spatial AVD are extracted from each sample. Various ML classifiers, including k-nearest neighbor (KNN), support vector machine (SVM), decision tree (DT), random forest (RF), Gaussian naive bayes (GNB), and artificial neural network (ANN), are trained on normalized features and tested under normal and noisy conditions. Results in Table 3.1 demonstrate that ML-based classifiers are accurate for data recorded in ideal conditions but fail to handle noisy data conditions. This shows that ML-based models are not robust to noise in data.

2.4.2 Deep learning based strategy for robust spatio-temporal analysis

After ML-based classification, this work is extended to DL-based analysis for accurate and robust spatio-temporal analysis of biospeckle data. Figure 2.9 shows the detailed strategy developed for the DL-based analysis. The main objectives of the study are as follows:

1. Development of DL-based models: Different DL networks, including neural networks, convolutional neural networks (CNN), long short-term memory networks (LSTM), and transfer learning techniques, are utilized to develop four different models for the spatio-temporal analysis of biospeckle data. These models are designed to capture both spatial and temporal information present in the data.

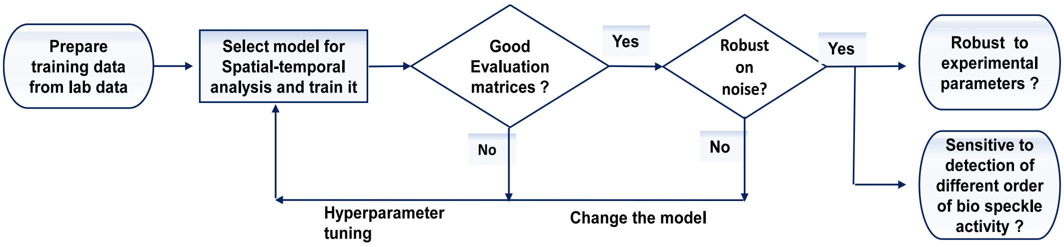

Figure 2.9: Flow chart of the strategy developed for robust spatio-temporal analysis of biospeckle data based on a DL-based framework.

2. Comparison of models for robustness: The developed models are compared to assess their robustness against noise in the data acquisition process. The models are evaluated under different noise conditions to determine their performance and identify the most robust model.

3. Impact of data parameters: This study further investigates the impact of experimental data parameters, such as frame size, frame rate, and the number of frames used, on the performance of the best robust model. This analysis helps understand the influence of these parameters on the model's accuracy and effectiveness.

4. Sensitivity to biospeckle activity of different orders: The robust model is further examined to evaluate its sensitivity in detecting biospeckle activity of different orders by evaluating its performance on an extended dataset with four different classes.

2.5 Deep learning networks used for spatio-temporal analysis

This Section describes the DL networks and techniques used for spatio-temporal analysis of biospeckle data, including neural networks, CNN, LSTM, 3-D convolutional neural network (3-D CNN), Convolutional LSTM (ConvLSTM) network, and transfer learning.

2.5.1 Neural Network

In a multi-layer perceptron (MLP) neural network, which is a type of feedforward neural network [46], there are typically three types of layers:

1. Input Layer: The input layer receives the input vector $[x_1, \ldots, x_p]$, which consists of the features of the data. Each neuron in the input layer represents a feature from the feature vector.

2. Hidden Layers: The hidden layers are between the input and output layers. They consist of multiple neurons or nodes that perform computations on the input data. Each neuron in the hidden layers is connected to all the neurons in the previous layer (either the input or the previous hidden layer) through weighted connections. These weights (w_{ij}) determine the strength of the connections between neurons. The input values from the previous layer are multiplied by the corresponding weights, and the weighted sums are then accumulated. The bias term (b_i) is added to the weighted sum to obtain a combined value (u_j). This combined value is passed through an activation function (Θ) to introduce non-linearity, and the output of the activation function (h_j) becomes the neuron's output in the hidden layer.

3. Output Layer: This layer receives the outputs from the last hidden layer as their inputs. It performs similar computations as the hidden layers, where each neuron in the output layer takes the combined outputs from the hidden layer neurons, computes a weighted sum with the corresponding weights, adds the bias term, passes it through an activation function, and produces the final output of the neural network.

Figure 2.10 represent a two layer MLP neural network and computations in a two layer MLP network are given in Equation 2.8.

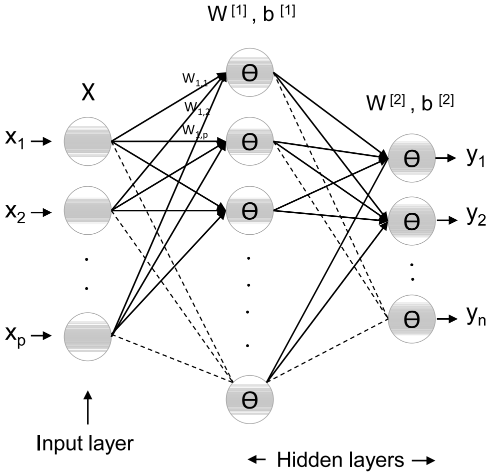

Figure 2.10: A two layer MLP neural network.

$$\begin{gathered}\boldsymbol{U}^{[1]}=\boldsymbol{W}^{[1]}\boldsymbol{X}+\boldsymbol{b}^{[1]},\boldsymbol{H}^{[1]}=\theta\left(\boldsymbol{U}^{[1]}\right),\\ \boldsymbol{U}^{[2]}=\boldsymbol{W}^{[2]}\boldsymbol{H}^{[1]}+\boldsymbol{b}^{[2]},\boldsymbol{H}^{[2]}=\theta\left(\boldsymbol{U}^{[2]}\right)=Y,\end{gathered} \tag{2.8}$$

where $\boldsymbol{W}^{[i]}$, $\boldsymbol{b}^{[i]}$ are weight and bias matrices associated with the i^{th} layer, respectively. $\boldsymbol{U}^{[i]}$ and $\boldsymbol{H}^{[i]}$ are vectorized version of u_i and h_i , $\boldsymbol{X}$ is vectorized input matrix with p number of features for each sample, and θ is activation function.

2.5.2 Convolutional neural networks

CNNs are developed to process information that is presented in various arrays, such as 1-D for signals and sequences, 2-D for images or audio spectrograms, and 3-D for videos or volumetric images. CNNs leverage four key ideas to process and extract features from these arrays effectively [47], which are described below.

1. Local connections: CNNs exploit the local spatial correlations in the input data. Each neuron in a convolutional layer is connected only to a small local receptive field in the previous layer, capturing local patterns and features. This local connectivity helps the network focus on specific regions of the input.

2. Shared weights: CNNs use shared parameters to detect the same feature across different spatial locations. The same set of weights (convolutional filters) is applied to different parts of the input data. This weight-sharing significantly reduces the number of parameters in the network, making it more efficient.

3. Pooling: Pooling layers reduce the spatial dimensions of the feature maps while preserving important information. Common pooling operations include max-pooling, which selects the maximum value from each local region, and average pooling, which computes the average value. Pooling helps to downsample the feature maps and make the network invariant to small translations and distortions in the input.

4. Many layers: CNNs are typically deep networks with multiple layers. The deep architecture allows the network to learn hierarchical representations of the input data, with each layer capturing increasingly complex and abstract features. Using many layers enables CNNs to solve complex problems by learning high-level representations.

CNNs are designed for image and spatial data analysis. They use a series of convolutional, pooling, and fully connected layers to extract features from the input data for target class recognition. In a CNN, the convolutional layers consist of units arranged in feature maps. Each unit in a feature map is connected to local patches or receptive fields in the feature maps of the previous layer through weights of convolutional filters. These filters, also known as kernels, perform convolution operations by sliding over the input feature maps and computing dot products between the filter weights and the input values within their receptive fields. By applying different filters, CNNs can extract various features, such as edges, textures, and patterns, from the input data.

Pooling layers are inserted between convolutional layers to downsample the feature maps and reduce their spatial dimensions. Pooling helps to combine semantically similar features into a single representative value while preserving valuable information. A popular CNN architecture (VGG16 [48]) is shown in Figure 2.11.

The parameters of the convolutional kernels (weights and biases) are learned during the training process using the backpropagation algorithm. During training, the network adjusts these parameters to minimize the error or loss between the predicted output and the true output labels. This process involves computing gradients and propagating them backward through the network to update the kernel weights and biases. By leveraging the hierarchical structure of convolutional layers and pooling layers, CNNs can automatically learn and extract relevant and discriminative features from the input data. This makes CNNs highly effective in image classification, object detection, and image segmentation tasks.

During the convolution operation in convolutional layers, the value at the position (x, y) in the j^{th} feature map in the i^{th} layer, denoted as F_{ij}^{xy}, is given as:

$$\mathrm{F}_{ij}^{xy} = \theta\left(b_{ij} + \sum_{m}\sum_{h=0}^{H_i-1}\sum_{w=0}^{W_i-1} w_{ijm}^{hw}\, \mathrm{F}_{(i-1)m}^{(x+h)(y+w)}\right), \tag{2.9}$$

$$\mathrm{F}_{ij} = \max_{j\in m}\left(\, \mathrm{F}_{(i-1)(j)}\right), \tag{2.10}$$

where θ is the activation function used after the convolutional operation, b_{ij} is the bias for the current feature map, m is number of feature maps in the $(i-1)^{th}$layer, w_{ijk}^{hw} is the value at the position (h, w) of the kernel connected to the k^{th} feature map, $max()$ is a max-pooling function. H_i and W_i are the height and width of the kernel, respectively.

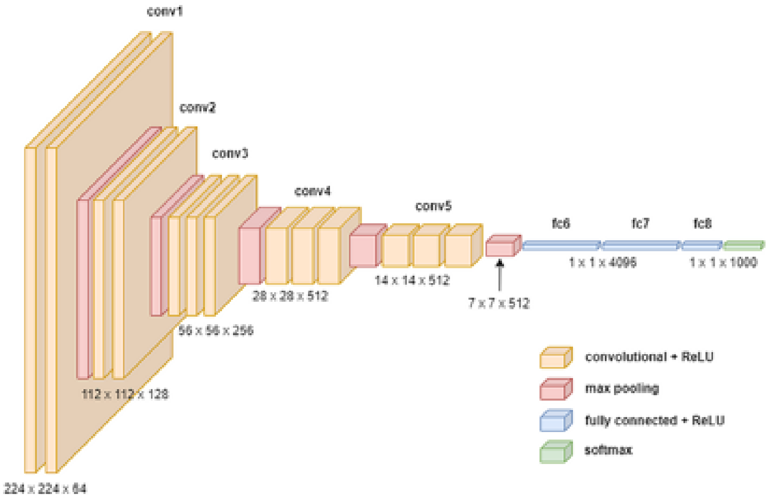

Figure 2.11: Architecture of VGG16 network.

2.5.3 Transfer learning

Transfer learning is a technique in deep learning that utilizes pre-trained models on large labeled datasets to address related tasks. It overcomes challenges associated with training large CNN models from scratch by leveraging the weights of pre-trained models. These models, already trained on datasets like ImageNet [49], possess knowledge of extracting general image features. The model can benefit from the learned features by initializing the CNN with these pre-trained weights, saving time and computational resources while improving performance on similar tasks.

Transfer learning indeed offers several advantages [50]. It saves time and computational resources by leveraging pre-trained models that already possess effective feature extraction capabilities. This results in enhanced performance as the pre-trained models capture valuable feature representations. Moreover, transfer learning enables improved generalization to new data, particularly when labeled examples are limited. By utilizing large pre-trained models as powerful feature extractors, transfer learning accelerates the development of new models while optimizing resource utilization.

Various pre-trained CNN models are available for transfer learning in popular deep learning frameworks. In our study, we have used several pre-trained models such as VGG16 [48], ResNet50 [51], DenseNet121 [52], Inception_V3, Inception_ResNet_V2 [53], EfficientNet [53], MobileNet [54], and Xception [55], which were pre-trained on the ImageNet dataset [49]. These models have already learned rich representations of features and are used as spatial feature extractors in stage 1 of Model 2 described in Section 2.6.2.

2.5.4 Long short-term memory network

Traditional deep neural networks, such as feedforward neural network and CNNs, assume that inputs and outputs are independent. However, for sequential data, the output at a given time step depends on the current and previous inputs within the sequence. Recurrent Neural Networks (RNNs) are specifically designed to handle sequential data by incorporating a "memory" mechanism. In RNNs, each neuron in a layer receives input from the current and previous time steps, allowing the network to retain information from previous inputs. This enables RNNs to model temporal dependencies and capture the sequential nature of the data. One key aspect of RNNs is that they share the same weight parameters across all time steps within a layer.

LSTM is a special type of RNN architecture that addresses some of the limitations of traditional RNNs, such as the vanishing gradient problem. The LSTM architecture includes memory cells (denoted as c^t) that store and propagate information across different time steps. These memory cells are controlled by parameterized gates. The input gate (denoted as i^t) controls the flow of new information into the memory cell . The forget gate (denoted as f^t) determines whether or not the previous cell state c^{t-1} should be forgotten or retained. The output gate (denoted as o^t) determines whether the current cell output c^t should be propagated to the final state h^t [56]. Figure 2.12 represents a single LSTM cell. Different configurations of deep LSTM networks can be formed by combining LSTM cells based on sequential data and the task at hand. One such network is shown in Figure 2.13.

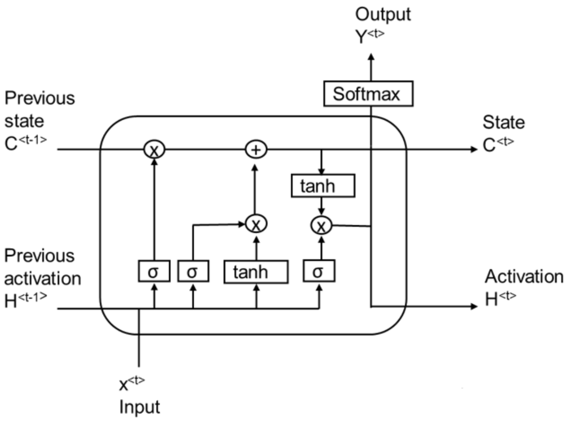

Figure 2.12: Block diagram of single LSTM cell.

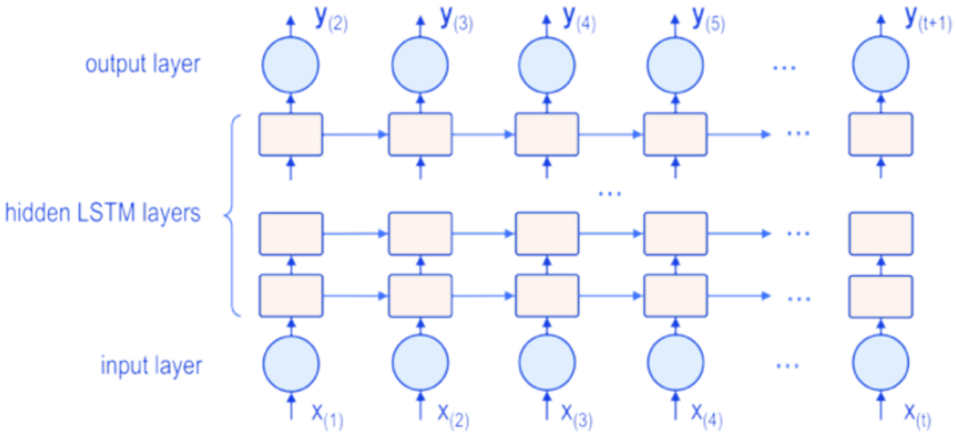

Figure 2.13: A typical deep LSTM network.

The multivariate LSTM structure consists of 1-D vectors for input, cell output, and states, also referred to as fully connected LSTM (FC-LSTM) networks due to the dense connections between input-to-state and state-to-state transitions. The LSTM cell performs memory cell and gate computations using a set of operations, which are described as follows:

$$
\begin{aligned}
i^t &= \sigma\left(W_{xi}x^t + W_{hi}h^{t-1} + W_{ci}c^{t-1} + b_i\right), \\
f^t &= \sigma\left(W_{xf}x^t + W_{hf}h^{t-1} + W_{cf}c^{t-1} + b_f\right), \\
c^t &= f^t c^{t-1} + i^t tanh\left(W_{xc}x^t + W_{hc}h^{t-1} + b_c\right), \\
o^t &= \sigma\left(W_{xo}x^t + W_{ho}h^{t-1} + W_{co}c^{t-1} + b_o\right), \\
h^t &= o^t tanh\left(c^t\right),
\end{aligned}
\tag{2.11}
$$

where *tanh* is hyperbolic tangent function.

2.5.5 3-D Convolutional neural network

A 3-D CNN is an extension of the traditional 2-D CNN that enables extracting features from both the spatial and temporal dimensions of the input data. While 2-D CNNs focus solely on spatial features represented by 2-D feature maps, 3-D CNNs are designed to capture the temporal variations in data, making them suitable for tasks involving time-dependent information. 3-D CNNs have greatly succeeded in various applications, including video analysis, action recognition, medical imaging, and volumetric data analysis. By considering the temporal or volumetric information, they can capture spatio-temporal or volumetric features and learn complex patterns in the data, making them well-suited for biospeckle activity analysis.

By performing 3-D convolutions in CNNs, we can simultaneously compute features from both the spatial and temporal dimensions. This is achieved by convolving a 3-D kernel with the cube formed by stacking contiguous frames from the preceding layer, considering both the spatial and temporal dimensions. The result of this convolution operation is the generation of 3-D spatio-temporal feature maps, which capture the combined spatial and temporal information of the input data [57]. A typical 3-D CNN architecture is shown in Figure 2.14.

In 3-D convolution, the value at position (x, y, z) on the j^{th} feature map in the i^{th} layer is given by:

$$
\mathrm{F}_{ij}^{xyz} = \theta\left(b_{ij} + \sum_{m}\sum_{h=0}^{H_i-1}\sum_{w=0}^{W_i-1}\sum_{d=0}^{D_i-1} w_{ijm}^{hwd}\ \mathrm{F}_{(i-1)m}^{(x+h)(y+w)(z+d)}\right), \tag{2.12}
$$

where D_i is the size of the 3-D kernel along the temporal dimension, w_{ijm}^{hwd} is the $(h, w, d)^{th}$ value of the kernel connected to the m^{th} feature map in the previous layer.

2.5.6 Convolutional LSTM network

The FC-LSTM network has limitations in encoding spatial information. It exhibits high data redundancy for spatial data due to the dense connections in input-to-

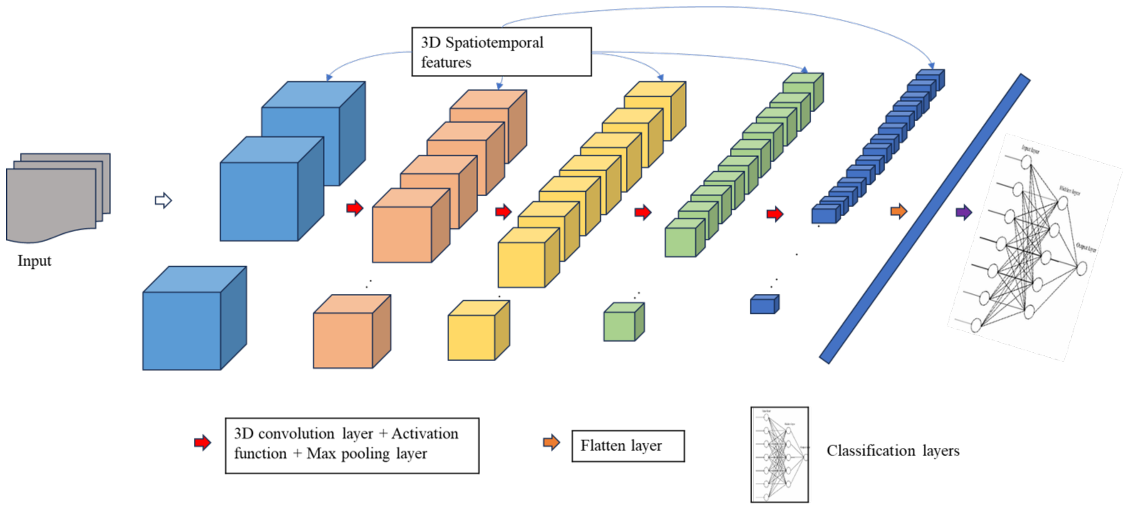

Figure 2.14: A typical 3-D CNN architecture.

state and state-to-state transitions. ConvLSTM networks have been introduced to overcome these limitations. These networks incorporate convolutional operations in both the input-to-state and state-to-state transitions, allowing them to encode spatial information and reduce data redundancy effectively [58].

In contrast to the FC-LSTM, which uses fully connected connections, the ConvLSTM operates on 3-D tensors. The inputs $[X_1 \ldots X_t]$, cell outputs $[C_1 \ldots C_t]$, hidden states $[H_1 \ldots H_t]$, and gates i^t, f^t, o^t of the ConvLSTM are all 3-D tensors, where the last two dimensions correspond to the spatial dimensions (rows and columns). This design allows the ConvLSTM network to effectively encode and process spatial information within the network, making it more suitable for spatio-temporal data analysis.

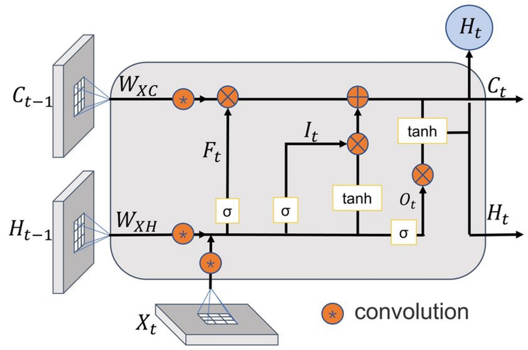

Figure 2.15: Block diagram of single ConvLSTM cell.

The key equations of ConvLSTM cell are mentioned in Equation 2.13, where '$*$' denotes the convolution operator.

$$\begin{aligned} i^t &= \sigma\left(W_{xi} * x^t + W_{hi} * h^{t-1} + W_{ci} * c^{t-1} + b_i\right) \\ f^t &= \sigma\left(W_{xf} * x^t + W_{hf} * h^{t-1} + W_{cf} * c^{t-1} + b_f\right) \\ c^t &= f^t c^{t-1} + i^t tanh\left(W_{xc} * x^t + W_{hc} * h^{t-1} + b_c\right) \\ o^t &= \sigma\left(W_{xo} * x^t + W_{ho} * h^{t-1} + W_{co} * c^{t-1} + b_o\right) \\ h^t &= o^t tanh\left(c^t\right) \end{aligned} \tag{2.13}$$

2.6 Architecture of four different models developed for analysis

In Section 2.5, various deep learning networks were discussed, each with different capabilities. CNNs excel at extracting spatial features from data, while LSTMs effectively process temporal features. Additionally, 3-D CNNs and ConvLSTM networks can extract spatial and temporal features simultaneously. Four different models were developed using these networks, which are described as:

2.6.1 Model 1 (Neural network with LSTM)

The end-to-end model for spatio-temporal analysis of biospeckle data consists of three stages:

1. Stage 1: In this stage, spatial features are extracted from the frames of video samples. These individual frames are used as input to a temporal distributed neural network, which includes densely connected layers. Dropout layers are inserted between the densely connected layers to prevent overfitting and improve generalization. The output of this stage is a set of 1-D vectors representing the spatial features extracted from the sample frames.

2. Stage 2: In the second stage, the extracted 1-D spatial features from stage 1 are used as input to the LSTM network. The LSTM network comprises multiple layers of LSTM units, which capture the temporal correlations in the data. By analyzing the sequential nature of the data, the LSTM network extracts the correlated temporal features.

3. Stage 3: The features extracted from stage 2, which have the spatial and temporal information captured by the previous stages, are fed to densely connected layers at stage 3 for classification.

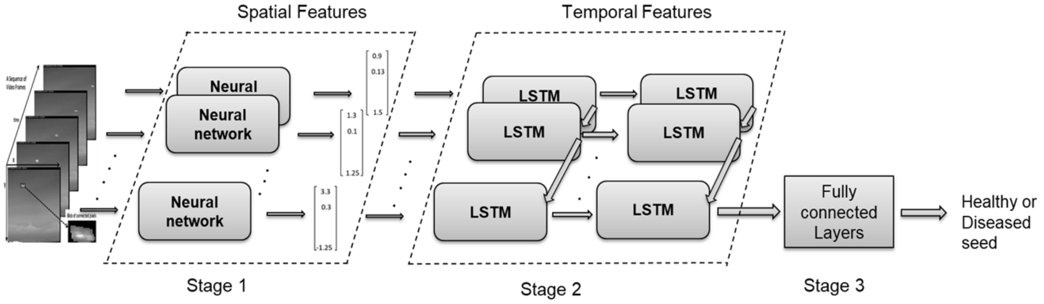

Figure 2.16: Model block diagram of neural network with LSTM network.

2.6.2 Model 2 (CNN with LSTM)

This model consists of CNN, LSTM, and a densely connected network in 3 stages described as:

1. Stage 1: In this stage, spatial features are extracted from the frames of a sample using a temporally distributed CNN network. The CNN network processes the frames and generates feature maps capturing spatial information. To convert the feature maps into 1-D vectors, a global average pooling layer is applied, which takes the average of each feature map along the spatial dimension. This process allows for the extraction of spatial features in the form of 1-D vectors.

2. Stage 2: This involves passing 1-D spatial features from stage 1 through an LSTM network to capture temporal dependencies and extract correlated temporal features.

3. Stage 3: At last stage, features from stage 2 are fed into densely connected layers for the final classification task, integrating spatial and temporal information for accurate predictions.

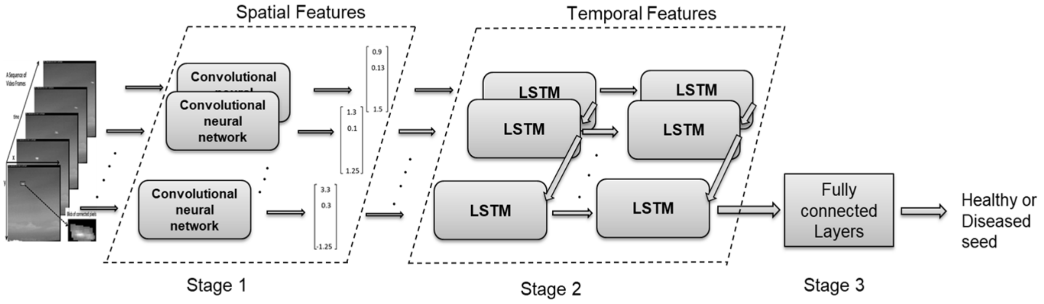

Figure 2.17: Model block diagram of CNN with LSTM network.

DL model	Stage 1	Stage 2	Stage 3
Model 1	Temporal distributed dense layers (48 and 32 nodes), two dropout layers with 10% dropout probability	Two LSTM layers (56 and 32 nodes), dropout (10%) in input-to-state and state-to-state dense connections	Two dense layers (16 and 1 nodes)
Model 2	Temporal distributed CNNs (pretrained and trained from scratch) followed by global average pooling2D layer	Two LSTM layers (64 and 32 nodes), dropout (15%) in input-to-state and state-to-state dense connections	Two dense layers (16 and 1 nodes)

Table 2.3: Network configuration details for model 1 and 2.

2.6.3 Model 3 (3-D Convolutional neural network)

The model architecture includes blocks, namely block 1, block 2, and block 3. Each block consists of a 3-D convolution layer, batch normalization, and a 3-D max pooling layer. These layers extract features from spatial and temporal dimensions, resulting in 3-D feature maps. 32 feature maps of size $(2, 4, 2)$ are obtained from third block. These feature maps are converted into a 1-D vector using a flatten layer. The classification layers utilize the resulting 1-D vector to make decisions for seeds.

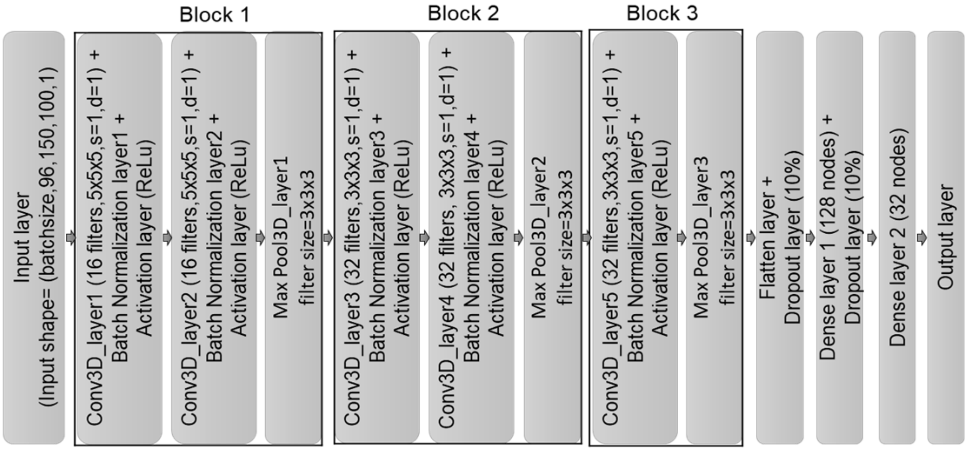

Figure 2.18: Model block diagram of 3-D CNN, where s is stride and d is dilation rate.

2.6.4 Model 4 (Convolutional LSTM network)

In the ConvLSTM model architecture, as depicted in Figure 2.19, the initial two blocks consist of three layers; the ConvLSTM layer, batch normalization, and the 3-D max pooling layer. The ConvLSTM layer processes the spatial data and produces

2-D feature maps for each frame, while the 3-D max pooling layer reduces the spatial dimensions of the feature maps. The output from the last unit of the ConvLSTM layer in block 3, containing encoded spatial and temporal features, undergoes spatial dimension reduction using the 2-D max pooling layer. Finally, the 2-D encoded spatial and temporal feature maps are converted into 1-D vectors through the 2-D average pooling layer for the classification task.

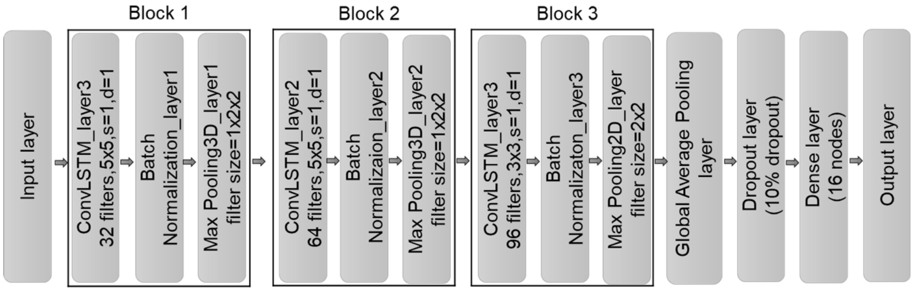

Figure 2.19: Model block diagram of Convolutional LSTM network.

2.7 Model performance evaluation

The model's performance is evaluated using standard measures such as classification accuracy, precision, recall, F1-score, and the area under the receiver operating characteristic curve (AUC). These measures are calculated using a confusion matrix, which contains information about true positives (TP), true negatives (TN), false positives (FP), and false negatives (FN).

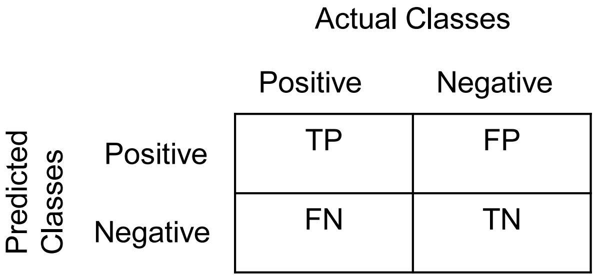

		Actual Classes	
		Positive	Negative
Predicted Classes	Positive	TP	FP
	Negative	FN	TN

Figure 2.20: Confusion matrix for binary classification.

Accuracy indicates the proportion of correctly predicted classes and gives an overall measure of the model's performance. Precision measures the accuracy of the model's predictions for the positive class, focusing on false positives. Recall, also known as sensitivity, provides insight into false negatives by measuring the proportion of positive instances correctly predicted by the model. Mathematical formulas for performance measures are given as:

$$Accuracy(\%) = \frac{TP + TN}{TP + TN + FP + FN} \times 100 \tag{2.14}$$

$$Precision(\%) = \frac{TP}{TP + FP} \times 100 \tag{2.15}$$

$$Recall(\%) = \frac{TP}{TP + FN} \times 100 \tag{2.16}$$

$$F1 - Score(\%) = \frac{2 \times Precision \times Recall}{Precision + Recall} \times 100 \tag{2.17}$$

$$True\ positive\ rate = \frac{TP}{TP + FN} \tag{2.18}$$

$$False\ positive\ rate = \frac{FP}{TN + FP} \tag{2.19}$$

The model's predictions are obtained by converting the output probabilities into class predictions using a cut-off threshold. However, evaluating performance based on a single threshold may not provide a complete understanding of the class separation. By using receiver operating characteristics (ROC) curve analysis, the model's performance can be assessed across various threshold values, plotting the true positive rate (TPR) against the false positive rate (FPR). The AUC measures the classifier's ability to differentiate between classes. A higher AUC value indicates better discrimination between positive and negative categories, offering an overall assessment of the model's performance across different classification thresholds.

Chapter 3

Result and discussion

The experimental dataset used in this study consists of 300 healthy and 300 infected soybean seed samples recorded using the experimental setup shown in Figure 2.1. The recorded biospeckle activity videos are processed to a frame size of 150x100 to remove unnecessary background information and reduce computational overhead during training. The dataset is divided into three subsets, with a ratio of 70% for the training set (424 samples), 15% for the validation set (88 samples), and 15% for the test set (88 samples). Each sample in the dataset contains a biospeckle activity record of 3 seconds captured at a frame rate of 32 fps. For robustness analysis, four additional test datasets with different types of noise are created using original test dataset described in Section 2.2. The DL-related work is conducted using TensorFlow [59] on the Google Colab Pro platform with a Tesla T4 graphics processing unit (GPU) with 32 GB of memory.

3.1 Machine Learning based classification for healthy and diseased seeds

As described in Section 2.4.1, for ML-based classification, we have extracted six different features such as temporal AVD, contrast, entropy, roughness, IM, and spatial AVD from each sample. Different classifiers, including KNN, SVM, DT, RF, GNB, and ANN, are trained on normalized features and tested under normal and noisy conditions. Results in Table 3.1 demonstrate that ML-based classifiers are accurate for data recorded in ideal conditions but fail to handle noisy data conditions. This shows that ML-based classifiers are not robust to noise in biospeckle data.

Table 3.1: Performance of different machine learning models on the test and noised test datasets.

ML models	Performance on test datasets						
	Original test dataset (in %)			Noised test datasets (Accuracy in %)			
	Accuracy	Precision	Recall	Gaussian Noised	Salt and Pepper Noised	Speckle Noised	Multiple Noise Added
GNB	89.77	81.25	100	51.13	89.77	51.13	51.13
SVM [1]	98.86	100	97.82	51.13	98.86	51.13	51.13
SVM [2]	98.86	97.82	100	51.13	48.86	51.13	51.13
DT	100	100	100	51.13	80.68	51.13	51.13
RF	100	100	100	51.13	93.18	51.13	51.13
KNN	98.86	100	97.82	55.68	78.40	51.13	54.54
ANN	98.86	100	97.82	48.86	48.86	48.86	48.86

[1] Radial basis function kernel of degree = 3 is used.

[2] Polynomial kernel of degree = 3 is used.

3.2 Performance and robustness of different deep learning models

In Section 2.6, all the models mentioned are trained using the experimental dataset without any data pre-processing. DL models are trained on the training data, and their performance is evaluated using the validation data after each epoch. The validation set is used during training to assess the model's performance and make decisions about hyperparameter tuning or model selection. It helps monitor the model's progress, detect overfitting or underfitting, and make adjustments to improve its generalization ability. Hyperparameter tuning involves finding the optimal values for hyperparameters, which are parameters set before the training process and cannot be learned from the data. Fine-tuning these hyperparameters can significantly impact the model's performance. Table 3.2 shows the hyperparameter details for different models. Their optimal values for DL models are mentioned in Figures 2.18 and 2.19, and Table 2.3.

During training, binary cross-entropy (Equation 3.1) is used as the cost function, and the Adam optimizer [60] is employed. The experimental data has a frame size of 150x100 pixels, a frame rate of 32 fps, and a total of 96 frames are utilized. The initial learning rate for the optimizer is set to 0.001. Different batch sizes of 32, 4, 6, and 2 are used for model 1, model 2, model 3, and model 4, respectively. The performance of the models on the test dataset, as well as on the noise test datasets, is summarized in Table 3.3. This provides an assessment of the model's performance on unseen data and their robustness to different noise conditions.

Binary cross-entropy ($loss_{bc}$) and categorical cross-entropy ($loss_{cc}$) loss functions

Hyperparameters for model 1	Number of layers in stage 1 and stage 2, number of nodes in layers of stage 1 and stage 2, dropout factor, regularization factor
Hyperparameters for model 2	Pre trained CNNs: [VGG16, Resnet50, Densenet121, Inception_V3, Efficient Net, Mobile Net, Inception_Resnet_V2, Xception],dropout factor, regularization factor
Hyperparameters for model 3	Filters size, number of filters, dropout and regularization in 3-D convolution and dense layers
Hyperparameters for model 4	Filters size, number of filters, dropout and regularization parameter in ConvLSTM layers, number of ConvLstm layers

Table 3.2: Hyperparameter details for different models.

are defined as:

$$loss_{bc} = -(y\log(p) + (1-y)\log(1-p)), \tag{3.1}$$

$$loss_{cc} = -\sum_{c=1}^{M} y_{o,c}\log(p_{o,c}), \tag{3.2}$$

where p is class predictions, y is class labels , and M is number of classes.

Figure 3.1 shows the loss and accuracy plots of training and validation for different models. In model 1, overfitting is observed due to the dense connections throughout the model, resulting in a large number of parameters. This leads to overfitting of the model on the training data, and its accuracy cannot be improved beyond 90% even after hyperparameter tuning. Model 2 replaces the dense layers with CNNs for spatio-temporalal feature extraction at stage 1 to address this issue, improving the model's performance on test data above 94%. However, when tested under noisy conditions, the model's performance degrades drastically, indicating that the model is not robust to noise in data. Different CNNs are explored for spatial feature extraction, and some are also trained from scratch to find whether the model performance can be improved in noisy conditions.

Tables 3.4 and 3.5 show that different variations of CNNs for spatial feature extraction and even training the model from scratch specifically for biospeckle data cannot improve the model performance in noisy conditions. The spatial information of frames is passed as 1-D vectors at stage 2 of the model for temporal processing resulting in loss of spatial information. To overcome this, spatio-temporal feature extraction or processing is required at each model layer instead of extracting both information separately at different parts of the network.

In contrast, the ConvLSTM model incorporates convolutional operations at all stages, preventing the loss of spatial information. The frame-wise spatial and temporal feature processing within the ConvLSTM layer enhances the robustness of the extracted features to noise. This model achieves an accuracy of 97.72% on the test dataset and demonstrates good performance on the noised test datasets as well, with

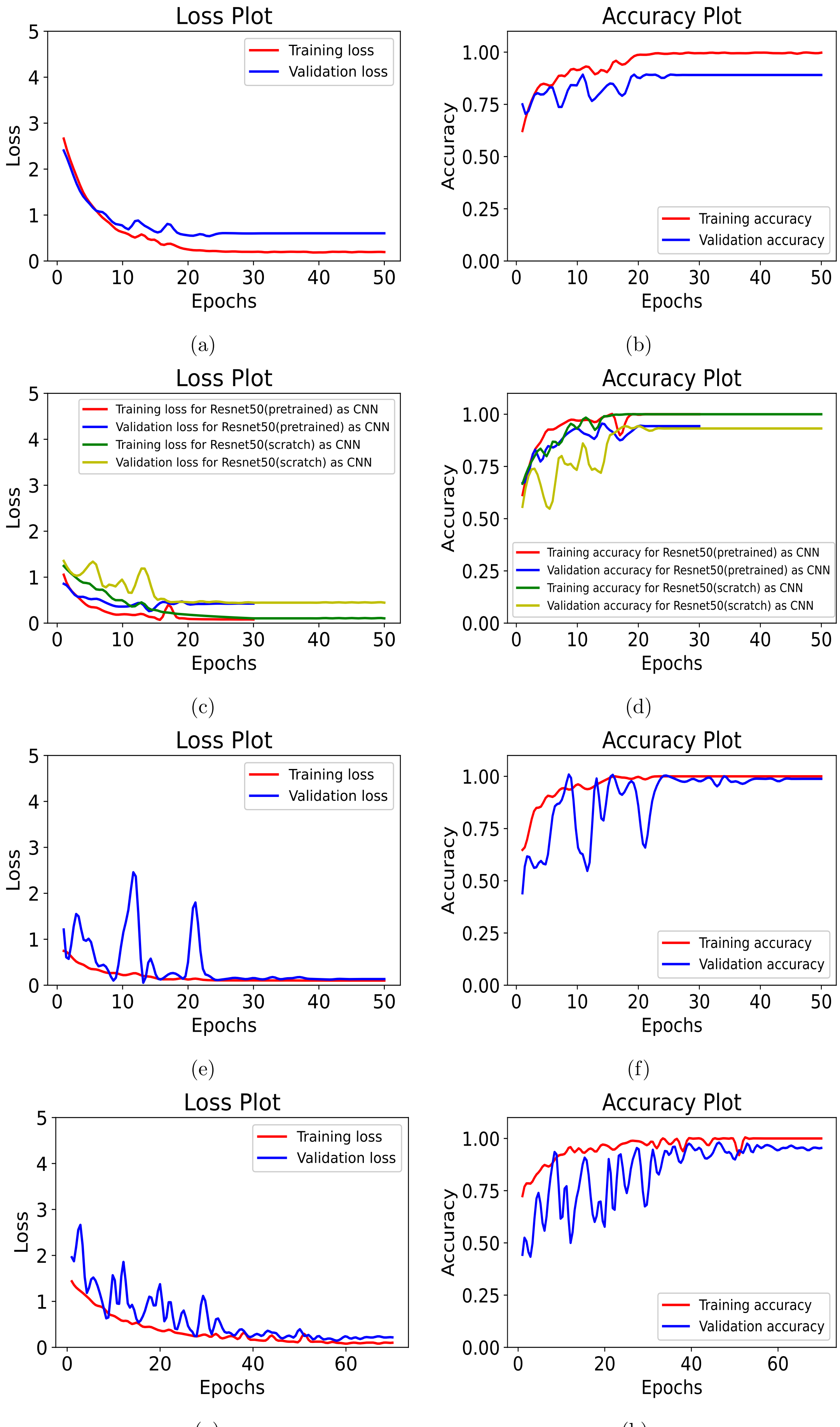

(a) (b)

(c) (d)

(e) (f)

(g) (h)

Figure 3.1: Loss and accuracy plots of training and validation for different models.

an accuracy of 97.72%, 94.31%, 98.86%, and 96.59% (Table 3.3). Figure 3.2 shows the ROC plots of different models on original and noised test datasets. ConvLSTM model has excellent class distinction capability having AUC values close to 1 for all test scenarios.

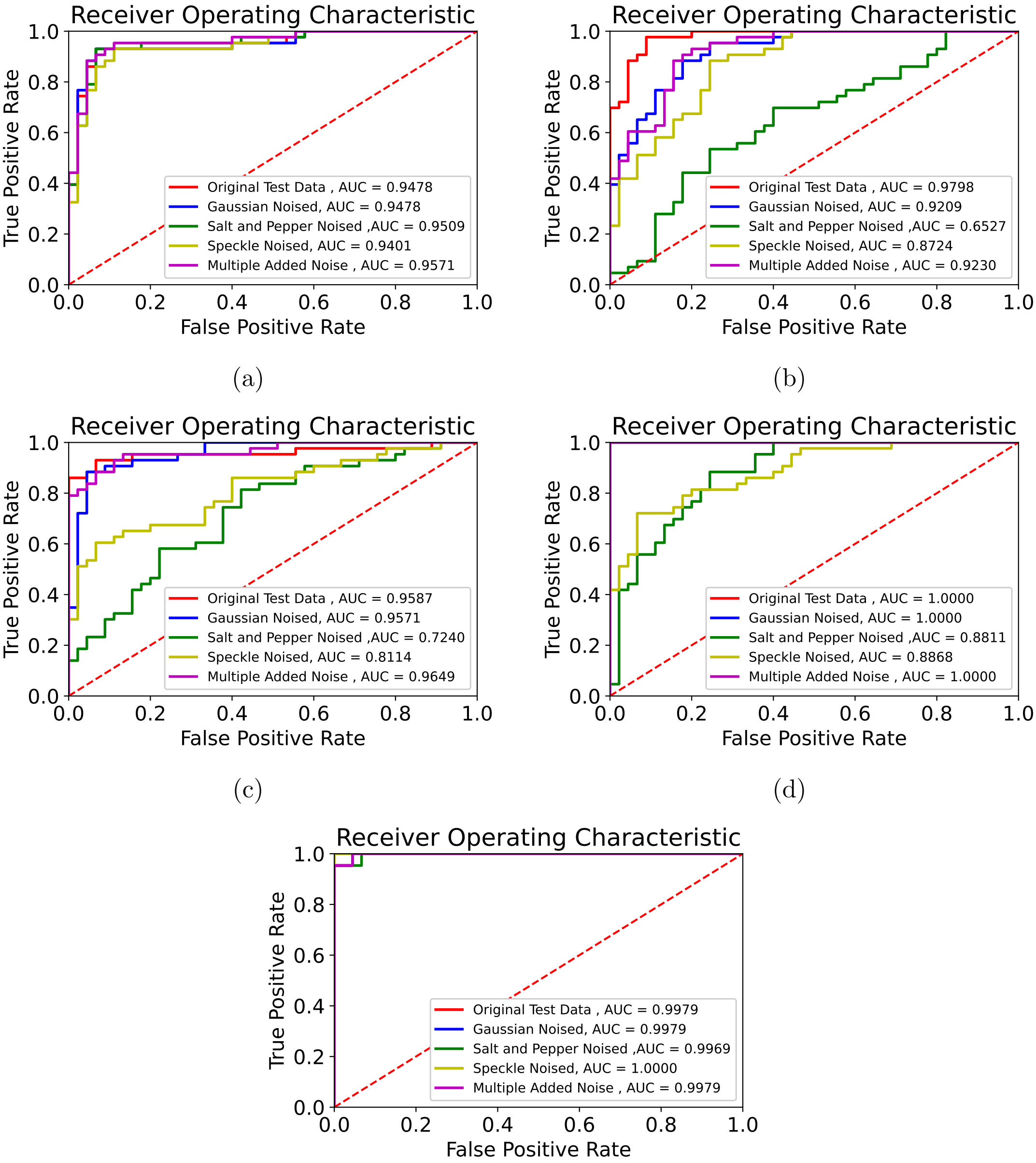

Figure 3.2: Comparison of different models using ROC plots (a) ROC plot of model 1, (b) ROC plot of model 2a, (c) ROC plot of model 2b, (d) ROC plot of model 3, (e) ROC plot of model 4.

Table 3.3: Performance of different models on the test and noised test datasets.

DL models	Performance on test datasets						
	Original test dataset (in %)			Noised test datasets (Accuracy in %)			
	Accuracy	Precision	Recall	Gaussian Noised	Salt and Pepper Noised	Speckle Noised	Multiple Noise Added
Model 1	89.77	86.95	93.02	90.90	75.00	88.63	84.09
Model 2a[1]	94.31	91.30	97.67	77.27	56.81	57.95	86.36
Model 2b[2]	93.18	93.02	93.02	80.68	56.81	68.18	89.77
Model 3	97.72	95.55	100	96.59	51.13	57.95	93.18
Model 4	**97.72**	**100**	**95.34**	**97.72**	**94.31**	**98.86**	**96.59**

[1] Model 2a uses pre-trained Resnet50 as CNN at stage 1.

[2] Model 2b uses Resnet50 trained from scratch as CNN at stage 1.

DL models	Performance on test datasets						
	Original test dataset (in %)			Noised test datasets (Accuracy in %)			
	Accuracy	Precision	Recall	Gaussian Noised	Salt and Pepper Noised	Speckle Noised	Multiple Noise Added
Vgg16	93.18	91.11	95.34	87.50	52.27	69.31	90.90
Resnet50	94.31	91.30	97.67	77.27	56.81	57.95	86.36
Densenet121	90.90	87.23	95.34	51.13	47.72	52.27	52.27
Inception_V3	89.77	85.41	95.34	63.63	47.72	48.86	80.68
Efficient Net	94.31	93.18	95.34	59.09	75.00	75.00	81.81
Mobile Net	97.72	95.55	100	62.50	78.40	59.09	78.40
Inception_Resnet_V2	47.72	0	0	44.31	50.00	36.36	43.18
Xception	93.18	91.11	95.34	79.54	47.72	48.86	85.22

Table 3.4: Performance of model 2 with different pretrained CNNs on test dataset and noised test datasets.

3.3 Performance of ConvLSTM model with experimental parameter variation of data

Image processing-based biospeckle analysis methods have relied on experimental data parameters, such as the number of temporal frames and selecting ROI, to achieve precise and accurate results. In contrast, DL-based biospeckle activity analysis offers the advantage of overcoming this dependency on data parameters, leading to more accurate outcomes. This study considered three significant factors; frame size, frame rate, and the number of frames. To investigate the effect of these parameters, different datasets were created from the original experimental dataset by varying these factors. To reduce computational and training time, the data was

DL models	Performance on test datasets						
	Original test dataset (in %)			Noised test datasets (Accuracy in %)			
	Accuracy	Precision	Recall	Gaussian Noised	Salt and Pepper Noised	Speckle Noised	Multiple Noise Added
Resnet50	93.18	93.02	93.02	80.68	56.81	68.18	89.77
Densenet121	93.18	93.02	93.02	78.40	48.86	55.68	95.45
Inception_V3	95.45	93.33	97.67	51.13	48.86	48.86	61.36
Mobile Net	88.63	86.66	90.69	73.86	51.13	73.86	79.54
Vgg16	51.13	0	0	51.13	51.13	51.13	51.13

Table 3.5: Performance of model 2 with different CNNs trained from scratch on test and noised test datasets.

normalized using z-score normalization. This normalization technique ensures that the data has a mean of zero and a standard deviation of one, thus bringing the data to a standard scale.

Z-score normalization is mathematically expressed as: Z = $\frac{X - \mu}{\sigma}$, where X is original data sample, μ and σ are mean and standard deviation of data sample, respectively.

In this study, experimental data parameters, including frame size, frame rate, and number of frames, were considered to assess their impact on the performance of the ConvLSTM model.

3.3.1 Variation in frame number

Three different datasets were created by keeping the frame size and frame rate constant and varying the number of frames used. The data parameters considered were a frame size of 150x100, a frame rate of 32 fps, and frames used of 96, 64, and 32. The training plots and the performance on the test dataset are shown in Figure 3.3 and Table 3.6, respectively.

Frames used	Performance on test dataset (in %)			
	Accuracy	Precision	Recall	F1 score
96	96.59	100	93.02	96.38
64	96.59	97.61	95.34	96.46
32	97.72	97.67	97.67	97.67

Table 3.6: Performance of ConvLSTM model on test dataset for frame number variation.

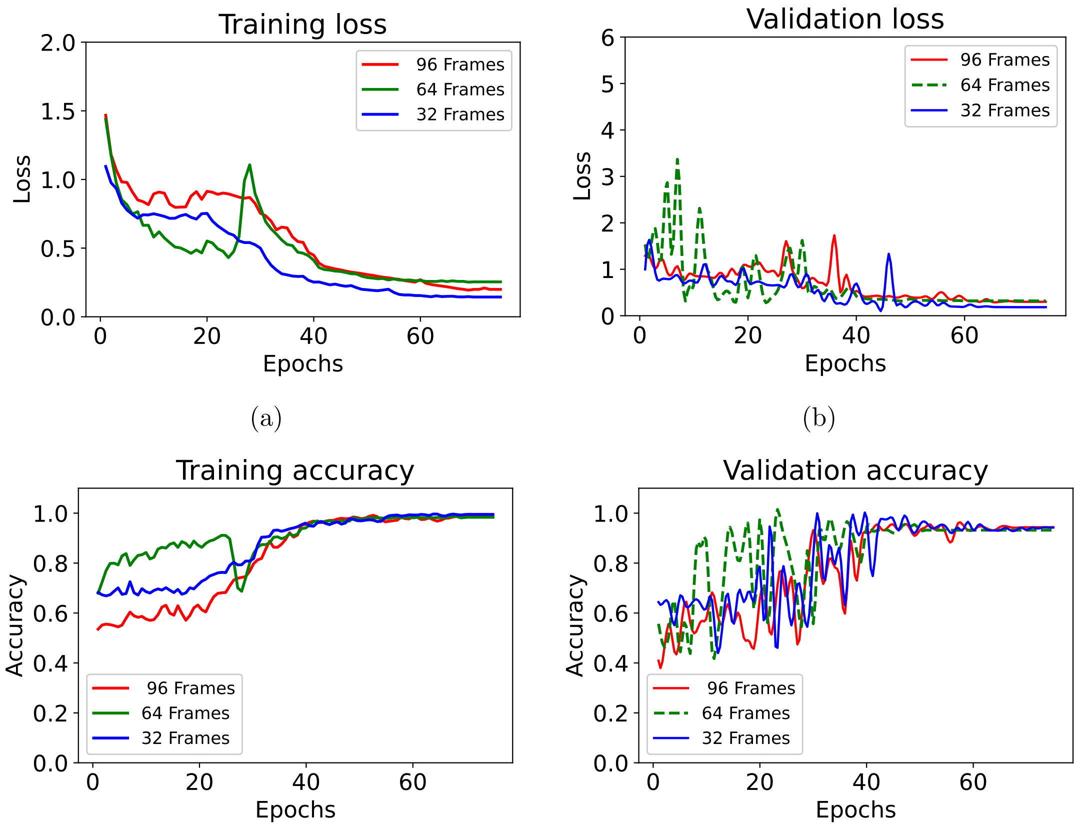

(a) (b)

(c) (d)

Figure 3.3: Training and validation plots for ConvLSTM model for frame number variation.

3.3.2 Variation in frame rate

The frame rate was varied while keeping the frame size and frames used at their maximum values. The frame rates considered were 32, 16, and 8. Figure 3.5 and Table 3.7 illustrate the training plots and the test dataset performance, respectively.

Frame rate	Performance on test dataset (in %)			
	Accuracy	Precision	Recall	F1 score
32	96.59	100	93.02	96.38
16	97.72	100	95.34	97.61
8	97.72	95.55	100	97.72

Table 3.7: Performance of ConvLSTM model on test dataset for frame rate variation.

3.3.3 Variation in frame size

The frame size was varied while maintaining a frame rate of 16 fps and using 48 frames. Different frame sizes considered were 100x100, 150x100, 150x150, and 175x175. The training plots and the performance on the test dataset are presented in Figure 3.4 and Table 3.8, respectively.

Frame size used	Performance on test dataset (in %)			
	Accuracy	Precision	Recall	F1 score
100x100	96.59	97.61	95.34	96.46
150x100	96.59	100	93.02	96.38
150x150	95.23	100	91.48	95.55
175x175	95.45	95.34	95.34	95.34

Table 3.8: Performance of ConvLSTM on test dataset for frame size variation.

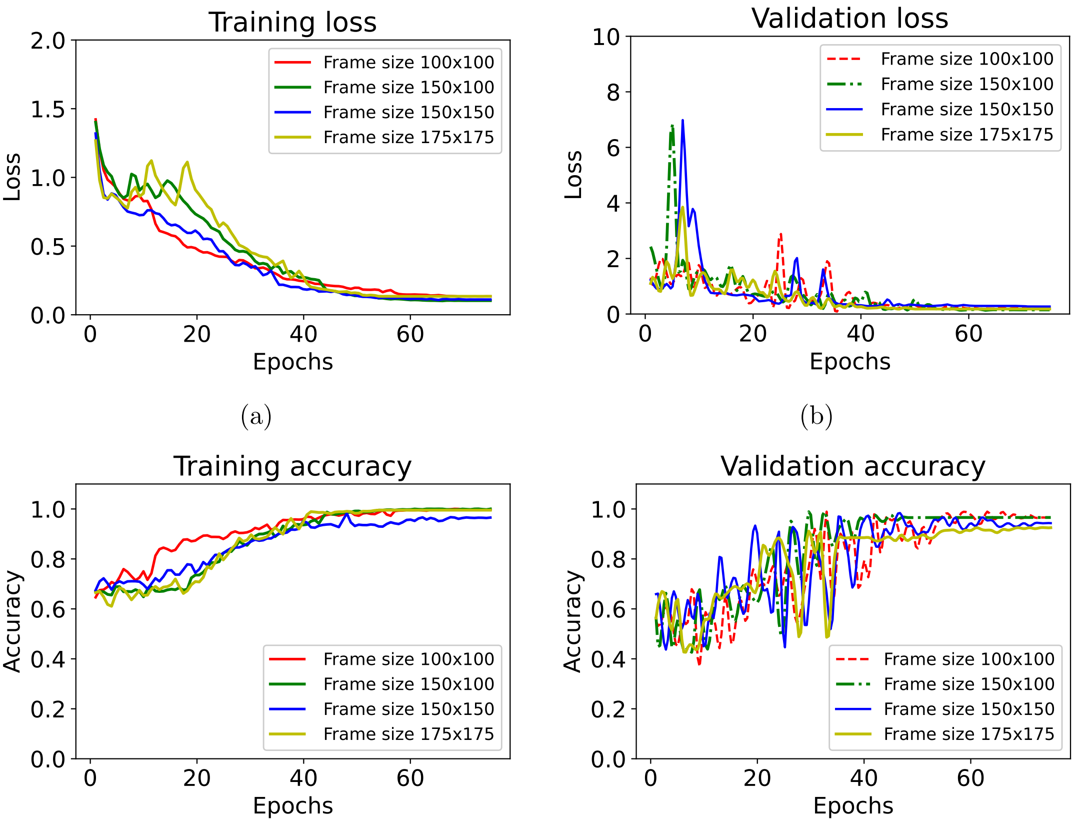

(a) (b)

(c) (d)

Figure 3.4: Training and validation plots for ConvLSTM model for frame size variation.

The results obtained from the ConvLSTM model demonstrate its robustness to variations in the experimental data parameters. The model achieves high accuracies of 97.72%, 97.72%, and 96.59% on the test dataset for the minimum values of the considered frame number, frame rate, and frame size, respectively. This indicates that even with a reduced number of frames (24) at a lower frame rate (8 fps) and a smaller spatial dimension (150x100), the model can still provide accurate results.

The findings from Tables 3.6, 3.7, and 3.8 highlight that the ConvLSTM model maintains a consistent performance with test accuracies ranging from 95.45% to 97.72% across different variations in data parameters. This information can be used

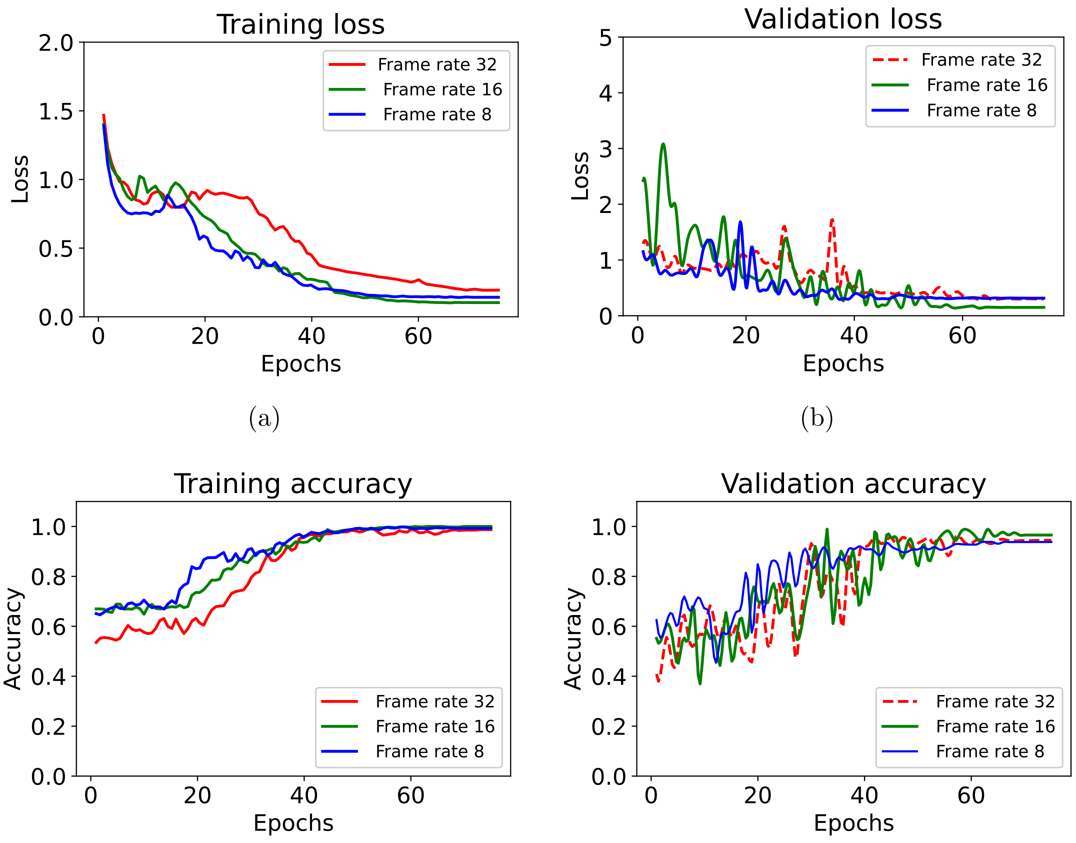

(a) (b)

(c) (d)

Figure 3.5: Training and validation plots for ConvLSTM model for frame rate variation.

to design a computationally efficient ConvLSTM network that inputs only 24 frames at 8 fps. By reducing the number of frames and the frame rate, the computational load on the GPU and the training time can be minimized without sacrificing the model's accuracy. These results offer valuable insights for optimizing the design and implementation of the ConvLSTM network, making it more efficient and practical for real-world applications in seed-borne disease detection using biospeckle imaging.

3.4 Sensitivity analysis of ConvLSTM model for biospeckle activity of different orders.

The extended dataset, as described in Section 2.3, which includes different orders of BSAI values, was used to evaluate the sensitivity of the ConvLSTM model. The multi-class dataset consists of 1080 samples, divided into training, validation, and test splits, with a ratio of 70/15/15 (%). The training dataset contains 756 samples, the validation dataset contains 162 samples, and the test dataset contains 162 samples. Each sample in the dataset represents a 3-second biospeckle activity data recorded at 32 fps. During training, the data is normalized using z-score normalization.

The ConvLSTM model is trained using categorical cross-entropy (Equation 3.2) as the cost function and the Adam optimizer with an initial learning rate of 0.001. The model is trained for 80 epochs with a batch size of 4. The data parameters used for training are frame size = 150x100, frame number = 48, and frame rate = 32 fps.

Classification report on test dataset				
Class name	Precision	Recall	F1-score	Test sample count
Class 0	98.00	100	99.00	46
Class 1	100	97.00	99.00	40
Class 2	100	100	100	41
Class 3	100	100	100	35
Average test accuracy = 99%				

Table 3.9: Performance of ConvLSTM model on test dataset for multi-class dataset.

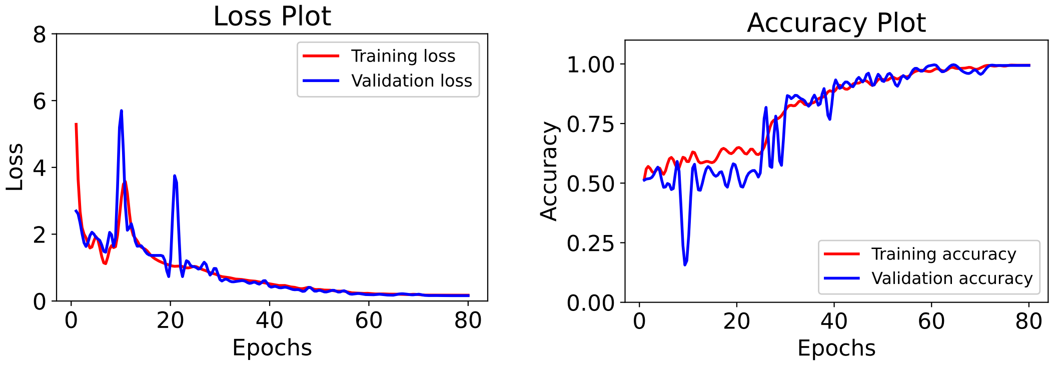

(a) (b)

Figure 3.6: Training and validation plots of ConvLSTM model on multi-class dataset.

The training and test results of the ConvLSTM model are presented in Figure 3.6 and Table 3.9, respectively. The model achieves an impressive average test accuracy of 99% on the multi-class data without hyperparameter tuning. This indicates that the ConvLSTM model is highly effective in identifying and classifying BSAI of different orders.

Chapter 4

Conclusions and Future Works

4.1 Conclusions

Accurate assessment of biospeckle activity in seed-borne fungal infection relies on integrating both spatial and temporal features. Combining the laser bio-speckle technique with DL has emerged as a promising approach for the real-time detection of fungal infection in seeds. This study utilizes DL-based methods to robustly analyze the spatio-temporal patterns of biospeckle data in soybean seeds. Among the DL models considered, the ConvLSTM model demonstrates exceptional performance, achieving an accuracy of 97.72% on the test dataset. Moreover, the model proves its resilience by maintaining high accuracies of 97.72%, 94.31%, 98.86%, and 96.59% on four distinct noised test datasets, highlighting its robustness to noise in data. Additionally, the ConvLSTM model is adaptable to variations in experimental parameters such as frame size, frame rate, and the number of frames used, indicating its versatility for different data settings.

Furthermore, this study extends the analysis to multi-class data, aiming to assess the sensitivity of the ConvLSTM model in detecting the bio-speckle activity of different orders. By training the model on a diverse dataset with varying levels of bio-speckle activity, the ConvLSTM model achieves an exceptional test accuracy of 99%. This result highlights the model's ability to accurately analyze and differentiate biospeckle activity of different orders. This model holds the potential for analyzing time-varying bio-speckle activity and facilitating seed quality assessment for diverse crop seeds simultaneously in the future.

4.2 Future Works

- The current study utilized a dataset specific to soybean seeds. To enhance the generalizability of the ConvLSTM model, future work could include a more diverse range of crop seeds, encompassing different species and varieties. The model's ability to assess seed quality across various agricultural contexts can be evaluated by incorporating multiple crop seeds.

- Real-time noise addition can be considered by performing experiments in non-ideal conditions, including uneven illumination conditions, and using a low-resolution CCD camera for recording data. Evaluating the model's performance on this recorded data will give more insights into the robustness of the model.
- Exploration of noise reduction techniques, such as denoising algorithms or data augmentation methods, can enhance the model's resilience and accuracy when applied to real-world scenarios with varying noise levels.
- The ConvLSTM model demonstrated adaptability to variations in frame size, frame rate, and frames used. However, future work can investigate optimizing these experimental parameters to determine the most efficient and effective configurations. This optimization process can lead to a computationally efficient ConvLSTM network that requires fewer frames and reduces training time while maintaining high accuracy.
- One of the significant advantages of the biospeckle technique combined with deep learning is its potential for the real-time detection of fungal infections in seeds. Future work can focus on developing a real-time implementation framework using the ConvLSTM model. Integration with suitable hardware platforms and optimization for efficient inference can be potentially applied in seed quality assessment during production or post-harvest stages.
- The application of the laser biospeckle technique and ConvLSTM model can be extended to investigate various agricultural aspects, such as seed and plant stress, fruit ripening, seed priming, and germination, by analyzing biospeckle activity variations over time.

Bibliography

[1] "Agriculture and food." https://www.worldbank.org/en/topic/agriculture/overview. Accessed: 2023-06-15.

[2] "Annual report 2020-21, department of agriculture, cooperation farmers' welfare." https://agricoop.nic.in/Documents/annual-report-2020-21.pdf. Accessed: 2023-06-15.

[3] A. Gull, A. A. Lone, and N. U. I. Wani, "Biotic and abiotic stresses in plants," *Abiotic and biotic stress in plants*, pp. 1–19, 2019.

[4] P. S. Thakur, V. Bhatia, L. S. Rajput, S. Rana, and S. Prakash, "Laser biospeckle technique for evaluating biotic stress on seed germination," in *2022 Workshop on Recent Advances in Photonics (WRAP)*, pp. 1–2, IEEE, 2022.

[5] "International: World oilseed production." http://soystats.com/international-world-oilseed-production/. Accessed: 2023-03-28.

[6] M. C. Pagano and M. Miransari, "The importance of soybean production worldwide," in *Abiotic and Biotic Stresses in Soybean Production*, vol. 1, ch. 1, pp. 1–26, U.K.: 1st ed. Oxford, 2016.

[7] "World soybean production." https://www.sopa.org/statistics/world-soybean-production/. Accessed: 2023-06-15.

[8] T. Talaviya, D. Shah, N. Patel, H. Yagnik, and M. Shah, "Implementation of artificial intelligence in agriculture for optimisation of irrigation and application of pesticides and herbicides," *Artificial Intelligence in Agriculture*, vol. 4, pp. 58–73, 2020.

[9] J. Y. Tan, P. J. Ker, K. Lau, M. Hannan, and S. G. H. Tang, "Applications of photonics in agriculture sector: A review," *Molecules*, vol. 24, no. 10, p. 2025, 2019.

[10] R. Kumar, A. Gupta, S. Srivastava, G. Devi, V. K. Singh, S. K. Goswami, M. S. Gurjar, and R. Aggarwal, "Diagnosis and detection of seed-borne fungal phytopathogens," *Seed-Borne Diseases of Agricultural Crops: Detection, Diagnosis & Management*, pp. 107–142, 2020.

[11] V. Mancini, S. Murolo, and G. Romanazzi, "Diagnostic methods for detecting fungal pathogens on vegetable seeds," *Plant Pathology*, vol. 65, no. 5, pp. 691–703, 2016.

[12] T. A. Matveyeva, R. M. Sarimov, A. V. Simakin, M. E. Astashev, D. E. Burmistrov, V. N. Lednev, P. A. Sdvizhenskii, M. Y. Grishin, S. M. Pershin, N. O. Chilingaryan, *et al.*, "Using fluorescence spectroscopy to detect rot in fruit and vegetable crops," *Applied Sciences*, vol. 12, no. 7, p. 3391, 2022.

[13] M.-Y. Shin, C. G. Viejo, E. Tongson, T. Wiechel, P. W. Taylor, and S. Fuentes, "Early detection of verticillium wilt of potatoes using near-infrared spectroscopy and machine learning modeling," *Computers and Electronics in Agriculture*, vol. 204, p. 107567, 2023.

[14] C. Baratto, G. Ambrosio, G. Faglia, and M. Turina, "Early detection of esca disease in asymptomatic vines by raman spectroscopy," *IEEE Sensors Journal*, vol. 22, no. 23, pp. 23286–23292, 2022.

[15] A. Soni, Y. Dixit, M. M. Reis, and G. Brightwell, "Hyperspectral imaging and machine learning in food microbiology: Developments and challenges in detection of bacterial, fungal, and viral contaminants," *Comprehensive Reviews in Food Science and Food Safety*, vol. 21, no. 4, pp. 3717–3745, 2022.

[16] F. Tao, H. Yao, Z. Hruska, L. W. Burger, K. Rajasekaran, and D. Bhatnagar, "Recent development of optical methods in rapid and non-destructive detection of aflatoxin and fungal contamination in agricultural products," *Trends in Analytical Chemistry (TrAC)*, vol. 100, pp. 65–81, 2018.

[17] P. S. Thakur, B. Tiwari, A. Kumar, B. Gedam, V. Bhatia, O. Krejcar, M. Dobrovolny, J. Nebhen, and S. Prakash, "Deep transfer learning based photonics sensor for assessment of seed-quality," *Computers and Electronics in Agriculture*, vol. 196, p. 106891, 2022.

[18] Z. Kalyzhner, O. Levitas, F. Kalichman, R. Jacobson, and Z. Zalevsky, "Photonic human identification based on deep learning of back scattered laser speckle patterns," *Optics Express*, vol. 27, no. 24, pp. 36002–36010, 2019.

[19] Z. Zalevsky, Y. Beiderman, I. Margalit, S. Gingold, M. Teicher, V. Mico, and J. Garcia, "Simultaneous remote extraction of multiple speech sources and heart beats from secondary speckles pattern," *Optics Express*, vol. 17, no. 24, pp. 21566–21580, 2009.

[20] A. Zdunek, A. Adamiak, P. M. Pieczywek, and A. Kurenda, "The biospeckle method for the investigation of agricultural crops: A review," *Optics and Lasers in Engineering*, vol. 52, pp. 276–285, 2014.

[21] Z. Li, P. Zhong, X. Tang, J. Ling, J. Chen, and G. He, “Effect of the speckle size on the quality of speckle pattern in dspi system,” *IEEE Access*, vol. 7, pp. 115010–115022, 2019.

[22] J. Moreira, R. Cardoso, and R. Braga, “Quality test protocol to dynamic laser speckle analysis,” *Optics and Lasers in Engineering*, vol. 61, pp. 8–13, 2014.

[23] R. Arizaga, M. Trivi, and H. Rabal, “Speckle time evolution characterization by the co-occurrence matrix analysis,” *Optics and Laser Technology*, vol. 31, no. 2, pp. 163–169, 1999.

[24] R. Braga, C. Nobre, A. Costa, T. Sáfadi, and F. Da Costa, “Evaluation of activity through dynamic laser speckle using the absolute value of the differences,” *Optics Communications*, vol. 284, no. 2, pp. 646–650, 2011.

[25] A. Oulamara, G. Tribillon, and J. Duvernoy, “Biological activity measurement on botanical specimen surfaces using a temporal decorrelation effect of laser speckle,” *Journal of Modern Optics*, vol. 36, no. 2, pp. 165–179, 1989.

[26] R. A. Braga Jr, R. J. González-Peña, D. C. Viana, and F. P. Rivera, “Dynamic laser speckle analyzed considering inhomogeneities in the biological sample,” *Journal of Biomedical Optics*, vol. 22, no. 4, pp. 045010–045010, 2017.

[27] I. Passoni, A. Dai Pra, H. Rabal, M. Trivi, and R. Arizaga, “Dynamic speckle processing using wavelets based entropy,” *Optics Communications*, vol. 246, no. 1-3, pp. 219–228, 2005.

[28] H. Fujii, K. Nohira, Y. Yamamoto, H. Ikawa, and T. Ohura, “Evaluation of blood flow by laser speckle image sensing. part 1,” *Applied Optics*, vol. 26, no. 24, pp. 5321–5325, 1987.

[29] R. A. Arizaga, N. L. Cap, H. J. Rabal, and M. Trivi, “Display of local activity using dynamical speckle patterns,” *Optical Engineering*, vol. 41, pp. 287–294, 2002.

[30] G. Richards and J. Briers, “Laser speckle contrast analysis (lasca): A technique for measuring capillary blood flow using the first order statistics of laser speckle patterns,” in *IEE Colloquium on Biomedical Applications of Photonics*, pp. 11–1, IET, 1997.

[31] A. Chatterjee, P. Singh, V. Bhatia, and S. Prakash, “A low-cost optical sensor for secured antispoof touchless palm print biometry,” *IEEE sensors letters*, vol. 2, no. 2, pp. 1–4, 2018.

[32] M. Javaid, A. Haleem, I. H. Khan, and R. Suman, “Understanding the potential applications of artificial intelligence in agriculture sector,” *Advanced Agrochem*, vol. 2, no. 1, pp. 15–30, 2023.

[33] A. Géron, *Hands-on machine learning with Scikit-Learn, Keras, and TensorFlow: Concepts, tools, and techniques to build intelligent systems.* ” O’Reilly Media, Inc.”, 2019.

[34] P. Singh, A. Chatterjee, L. S. Rajput, S. Rana, S. Kumar, V. Nataraj, V. Bhatia, and S. Prakash, “Development of an intelligent laser biospeckle system for early detection and classification of soybean seeds infected with seed-borne fungal pathogen (colletotrichum truncatum),” *Biosystems Engineering*, vol. 212, pp. 442–457, 2021.

[35] A. Rahmanian, S. A. Mireei, S. Sadri, M. Gholami, and M. Nazeri, “Application of biospeckle laser imaging for early detection of chilling and freezing disorders in orange,” *Postharvest Biology and Technology*, vol. 162, p. 111118, 2020.

[36] P. S. Thakur, A. Kumar, B. Tiwari, B. Gedam, V. Bhatia, S. Rana, and S. Prakash, “Machine learning based biospeckle technique for identification of seed viability using spatio-temporal analysis,” in *2022 Workshop on Recent Advances in Photonics (WRAP)*, pp. 1–2, IEEE, 2022.

[37] A. Wu, J. Zhu, and T. Ren, “Detection of apple defect using laser-induced light backscattering imaging and convolutional neural network,” *Computers and Electrical Engineering*, vol. 81, p. 106454, 2020.

[38] T. R. Boufleur, M. Ciampi-Guillardi, Í. Tikami, F. Rogério, M. R. Thon, S. A. Sukno, N. S. Massola Junior, and R. Baroncelli, “Soybean anthracnose caused by colletotrichum species: Current status and future prospects,” *Molecular Plant Pathology*, vol. 22, no. 4, pp. 393–409, 2021.

[39] P. S. Thakur, A. Chatterjee, L. S. Rajput, S. Rana, V. Bhatia, and S. Prakash, “Laser biospeckle technique for characterizing the impact of temperature and initial moisture content on seed germination,” *Optics and Lasers in Engineering*, vol. 153, p. 106999, 2022.

[40] Y. Fan, L. Zhang, H. Guo, H. Hao, and K. Qian, “Image processing for laser imaging using adaptive homomorphic filtering and total variation,” in *Photonics*, vol. 7, p. 30, MDPI, 2020.

[41] K. Basak, M. Mahadevappa, and P. K. Dutta, “Multiscale noise-adaptive homomorphic filtering based speckle denoising in laser speckle imaging,” in *2013 Fourth National Conference on Computer Vision, Pattern Recognition, Image Processing and Graphics (NCVPRIPG)*, pp. 1–5, IEEE, 2013.

[42] M. Konnik and J. Welsh, "High-level numerical simulations of noise in ccd and cmos photosensors: review and tutorial," *arXiv preprint arXiv:1412.4031*, 2014.

[43] A. K. Boyat and B. K. Joshi, "A review paper: noise models in digital image processing," *arXiv preprint arXiv:1505.03489*, 2015.

[44] A. L. Dai Pra, G. J. Meschino, M. N. Guzmán, A. G. Scandurra, M. A. González, C. Weber, M. Trivi, H. Rabal, and L. I. Passoni, "Dynamic speckle image segmentation using self-organizing maps," *Journal of Optics*, vol. 18, no. 8, p. 085606, 2016.

[45] A. Chatterjee, P. Singh, V. Bhatia, and S. Prakash, "An efficient automated biospeckle indexing strategy using morphological and geo-statistical descriptors," *Optics and Lasers in Engineering*, vol. 134, p. 106217, 2020.

[46] I. El-Feghi, A. Tahar, and M. Ahmadi, "Efficient features extraction for fingerprint classification with multi layer perceptron neural network," in *ISSCS 2011-International Symposium on Signals, Circuits and Systems*, pp. 1–4, IEEE, 2011.

[47] Y. LeCun, Y. Bengio, and G. Hinton, "Deep learning," *Nature*, vol. 521, no. 7553, pp. 436–444, 2015.

[48] K. Simonyan and A. Zisserman, "Very deep convolutional networks for large-scale image recognition," *arXiv preprint arXiv:1409.1556*, 2014.

[49] J. Deng, W. Dong, R. Socher, L.-J. Li, K. Li, and L. Fei-Fei, "Imagenet: A large-scale hierarchical image database," in *Proceedings of the IEEE Conference on Computer Vision and Pattern Recognition (CVPR)*, pp. 248–255, 2009.

[50] J. Chen, J. Chen, D. Zhang, Y. Sun, and Y. A. Nanehkaran, "Using deep transfer learning for image-based plant disease identification," *Computers and Electronics in Agriculture*, vol. 173, p. 105393, 2020.

[51] K. He, X. Zhang, S. Ren, and J. Sun, "Deep residual learning for image recognition," in *Proceedings of the IEEE Conference on Computer Vision and Pattern Recognition (CVPR)*, pp. 770–778, 2016.

[52] G. Huang, Z. Liu, L. Van Der Maaten, and K. Q. Weinberger, "Densely connected convolutional networks," in *Proceedings of the IEEE Conference on Computer Vision and Pattern Recognition (CVPR)*, pp. 4700–4708, 2017.

[53] M. Tan and Q. Le, "Efficientnet: Rethinking model scaling for convolutional neural networks," in *International Conference on Machine Learning (ICML)*, pp. 6105–6114, PMLR, 2019.

[54] A. G. Howard, M. Zhu, B. Chen, D. Kalenichenko, W. Wang, T. Weyand, M. Andreetto, and H. Adam, "Mobilenets: Efficient convolutional neural networks for mobile vision applications," *arXiv preprint arXiv:1704.04861*, 2017.

[55] F. Chollet, "Xception: Deep learning with depthwise separable convolutions," in *Proceedings of the IEEE Conference on Computer Vision and Pattern Recognition (CVPR)*, pp. 1251–1258, 2017.

[56] S. Hochreiter and J. Schmidhuber, "Long short-term memory," *Neural computation*, vol. 9, no. 8, pp. 1735–1780, 1997.

[57] S. Ji, W. Xu, M. Yang, and K. Yu, "3d convolutional neural networks for human action recognition," *IEEE Transactions on Pattern Analysis and Machine Intelligence*, vol. 35, no. 1, pp. 221–231, 2012.

[58] X. Shi, Z. Chen, H. Wang, D.-Y. Yeung, W.-K. Wong, and W.-c. Woo, "Convolutional lstm network: A machine learning approach for precipitation nowcasting," *Advances in Neural Information Processing Systems (NIPS)*, vol. 28, 2015.

[59] M. Abadi, A. Agarwal, P. Barham, E. Brevdo, Z. Chen, C. Citro, G. S. Corrado, A. Davis, J. Dean, M. Devin, S. Ghemawat, I. Goodfellow, A. Harp, G. Irving, M. Isard, Y. Jia, R. Jozefowicz, L. Kaiser, M. Kudlur, J. Levenberg, D. Mané, R. Monga, S. Moore, D. Murray, C. Olah, M. Schuster, J. Shlens, B. Steiner, I. Sutskever, K. Talwar, P. Tucker, V. Vanhoucke, V. Vasudevan, F. Viégas, O. Vinyals, P. Warden, M. Wattenberg, M. Wicke, Y. Yu, and X. Zheng, "TensorFlow: Large-scale machine learning on heterogeneous systems," 2015. Software available from tensorflow.org.

[60] D. P. Kingma and J. Ba, "Adam: A method for stochastic optimization," *arXiv preprint arXiv:1412.6980*, 2014.

List of Publications

In Refereed Journals

[1] N. Kaler, V. Bhatia, and A. K. Mishra,“Deep Learning-Based Robust Analysis of Laser Bio-Speckle Data for Detection of Fungal-Infected Soybean Seeds” in *IEEE Access*, vol. 11, pp. 89331-89348, 2023.